Computational and Experimental Fluid Dynamics of Jet Loop Reactor

Channamallikarjun S. Mathpati, Sagar S. Deshpande, and Jyeshtharaj B. Joshi
Dept. of Chemical Engineering, Institute of Chemical Technology, Matunga, Mumbai 400 019, India

DOI 10.1002/aic.11853
Published online July 30, 2009 in Wiley InterScience (www.interscience.wiley.com).

A computational analysis using standard k-ε model, RSM and LES has been carried out for jet loop reactors (JLR) to investigate the mean and turbulence quantities. These simulations have revealed that the flow in JLR was different from the self-similar round jets. RSM and LES showed better agreement with PIV measurements compared with standard k-ε model. The modeled turbulence production and transport in k-ε model overpredicted those estimated from LES data. To reduce the limitations, modified k-ε models have been evaluated for JLR. Also, a hybrid k-ε model has been suggested, which was found to perform better than other modified k-ε models. This model was also found to hold for stirred tank reactors (STRs). Mixing time analysis has been carried out for JLR and STR at same power consumption. It has been shown that JLR can be inferior to STR if proper nozzle diameter is not selected. © 2009 American Institute of Chemical Engineers *AIChE J*, 55: 2526–2544, 2009

Keywords: jet loop reactor, turbulence models, CFD, k-ε model, RSM, LES, PIV, stirred tank reactor, mixing time

Introduction

Jet loop reactors (JLR) are frequently used in the process industry as an alternative to impeller mixers due to the existence of relatively intense convective flow leading to enhanced rate of macro-mixing at the same power consumption. In a JLR, part of the content of the vessel is recirculated by drawing it through a pump and returning it at high speed through a nozzle. The resulting high speed jet entrains some of the surrounding liquid and creates a circulation pattern within the vessel. Figure 1 shows the schematic of JLR and the inside flow pattern. This equipment is easy to install, operate, and maintain with no requirement of any structural reinforcement of the tank, and it is normally cheaper in cost, when compared with conventional stirred tank reactors. Furthermore, JLRs also give improved heat and mass transfer rates.[1] Because of these advantages, JLRs are widely used in environmental and biological applications[2,3] and in nuclear reactors.[1] In addition, JLRs are used for fast, competitive-consecutive reactions having a mixing sensitive product distribution.[4,5]

JLRs find their genesis in widely studied round axi-symmteric jets in which a jet is injected in a stagnant pool of same or miscible liquid. In this process, the ambient fluid gets carried along with jet by viscous drag at the outer layer of jet causing mixing of these two fluids. One more interesting feature of these flows is self-similarity. When the profiles of axial and radial velocity as well as energy dissipation rate are normalized by the centerline velocity $\langle u_{2,\mathcal{C}} \rangle$ and $r_{1/2}$ (the radial distance at which axial velocity is half of the centerline velocity), they fall on a single curve for different axial locations (for $x_2/d > 30$).[6–8] However, the designs implemented in the industry do not have self-similar pattern due to larger nozzle diameters, smaller tank diameter, and smaller extent in axial direction (maximum $x_2/d \sim 10$ in the present case). The major work in JLR comprises of study of flow pattern, mixing time, and development of correlations using experimental[9–20] and computational tools.[21–23] The comprehensive measurements and computational fluid dynamics (CFD) simulations of flow pattern in JLR (three components of mean velocity, turbulent kinetic energy, and dissipation rate) is not available in the published literature. Such measurements and the

Correspondence concerning this article should be addressed to J. B. Joshi at jbj@udct.org

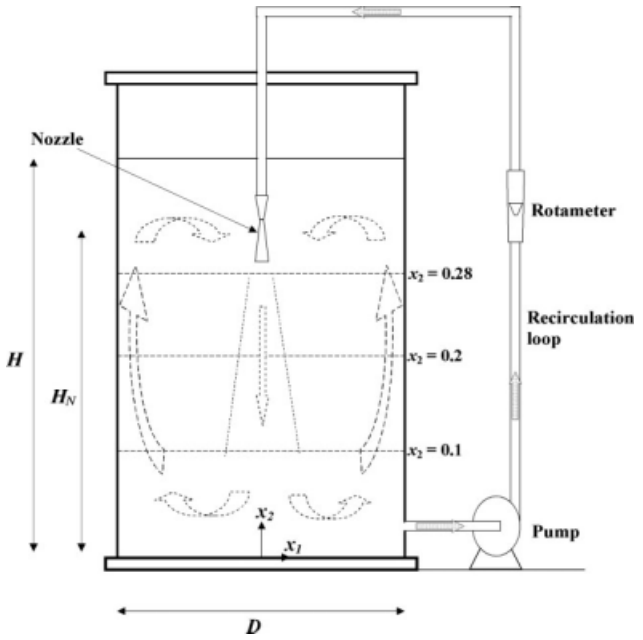

Figure 1. Schematic diagram of JLR.

comparison with simulations are required for JLRs to develop confidence in the designs. Therefore, it was thought desirable to undertake a systematic study using particle image velocimetry (PIV) and CFD using k-ε model, Reynolds stress model (RSM) and large eddy simulation (LES).

CFD

In CFD, the equations of continuity and motion should ideally be solved directly [direct numerical simulation (DNS)]. However, because of huge computational demand for flows in a variety of equipments, the equations of change are solved in combination with additional closure equations arising out of ensemble averaging (k-ε model and RSM) or space filtering (LES). The equations of change for a three-dimensional incompressible system can be represented in the following form[6]:

$$\frac{\partial u_i}{\partial x_i} = 0, \tag{1}$$

$$\rho \frac{\partial u_i}{\partial t} + \rho u_j \frac{\partial u_i}{\partial x_j} = -\frac{\partial p}{\partial x_i} + \frac{\partial}{\partial x_j}\left(\mu \frac{\partial u_i}{\partial x_j}\right). \tag{2}$$

Equations 1 and 2 on ensemble-averaging reduce to the following form:

$$\frac{\partial \langle u_i \rangle}{\partial x_i} = 0, \tag{3}$$

$$\rho \frac{\partial \langle u_i \rangle}{\partial t} + \rho \langle u_j \rangle \frac{\partial \langle u_i \rangle}{\partial x_j} = -\frac{\partial \langle p \rangle}{\partial x_i} + \frac{\partial}{\partial x_j}\left(\mu \frac{\partial \langle u_i \rangle}{\partial x_j} - \rho \left\langle u_i' u_j' \right\rangle\right). \tag{4}$$

The Reynolds stresses ($-\rho \partial \langle u_i' u_j' \rangle / \partial x_j$ in Eq. 4) arising out of ensemble-averaging procedure are modeled according to the Boussinesq hypothesis and given by:

$$-\rho \langle u_i' u_j' \rangle = \frac{2}{3} k \rho \delta_{ij} - \mu_t \left(\frac{\partial \langle u_i \rangle}{\partial x_j} + \frac{\partial \langle u_j \rangle}{\partial x_i}\right). \tag{5}$$

To close the system of equations, μ_t has been formulated in many ways in the literature in terms of zero, one, and two equation models. The most popular is the two equation model where μ_t is estimated from turbulent length and time scales. In the case of standard k-ε model, μ_t is estimated using turbulent kinetic energy (k) and rate of dissipation of turbulent kinetic energy (ε).

$$\mu_t = C_\mu \rho \frac{k^2}{\varepsilon}. \tag{6}$$

The values of k and ε are obtained by solving their transport equations,[24] which are listed in Table 1. However, the exact k *and* ε equations can not be solved directly, because they contain triple correlations of fluctuating velocity or ensemble-averaging of gradients of fluctuating velocities (Eqs. T1 and T3, Table 1). These terms can not be estimated directly and need modeling. Table 1 summarizes the modeling efforts.

First of all for simplification, the production term $(-\rho \langle u_i' u_j' \rangle (\partial \langle u_i \rangle / . \partial x_k))$ [term (c) in Eq. T1] is modeled as Reynolds stress times the strain rate $(\tau_{ij} \partial \langle u_i \rangle / \partial x_j)$ [term (c) in Eq. T2]. The turbulent transport due to pressure fluctuation $\left(\partial \langle p' u_k' \rangle / \partial x_k\right)$ [term (d) in Eq. T1] is neglected. The triple correlations of velocity fluctuation $\left(\partial \left((-1/2)\rho \langle u_i' u_i' u_k' \rangle\right) / \partial x_k\right)$ [term (d) in Eq. T1] are modeled using gradient diffusion hypothesis as $(\partial((\mu_t/\sigma_k)(\partial k/\partial x_k))/\partial x_k)$ [term (d) in Eq. T2].

The ε equation is modeled in an analogous way to k equation and using dimensional analysis. The production term in the exact dissipation equation [term (c) in Eqs. T3 and T4] is modeled as:

$$-2\mu\left(\left\langle \frac{\partial u_i'}{\partial x_j}\frac{\partial u_k'}{\partial x_j}\right\rangle + \left\langle \frac{\partial u_j'}{\partial x_i}\frac{\partial u_j'}{\partial x_k}\right\rangle\right)\frac{\partial \langle u_i \rangle}{\partial x_k} - 2\mu\left\langle u_k' \frac{\partial u_i'}{\partial x_j}\right\rangle \frac{\partial^2 \langle u_i \rangle}{\partial x_k \partial x_j} - 2\mu\left\langle \frac{\partial u_i'}{\partial x_k}\frac{\partial u_i'}{\partial x_m}\frac{\partial u_k'}{\partial x_m}\right\rangle \tag{7}$$

$$\approx \mu \frac{u^2}{L^2}\frac{\partial \langle u_i \rangle}{\partial x_j} \approx \frac{u}{L}\mu\frac{u}{L}\frac{\partial \langle u_i \rangle}{\partial x_j} \approx \frac{u}{L}\tau_{ij}\frac{\partial \langle u_i \rangle}{\partial x_j} \approx \frac{u^2}{t_s}\frac{1}{u^2}\tau_{ij}\frac{\partial \langle u_i \rangle}{\partial x_j} \approx \frac{\varepsilon}{k}\tau_{ij}\frac{\partial \langle u_i \rangle}{\partial x_j} \approx C_{\varepsilon 1}\frac{\varepsilon}{k}\tau_{ij}\frac{\partial \langle u_i \rangle}{\partial x_j}. \tag{8}$$

The modeling of turbulent transport term [term (d) in Eqs. T3 and T4] is given by

$$-\mu\left\langle u_j' \frac{\partial u_i'}{\partial x_m}\frac{\partial u_i'}{\partial x_m}\right\rangle - 2\upsilon\left\langle \frac{\partial p'}{\partial x_m}\frac{\partial u_j'}{\partial x_m}\right\rangle = \frac{\mu_t}{\sigma_\varepsilon}\frac{\partial \varepsilon}{\partial x_j}. \tag{9}$$

Further the modeling of dissipation term [term (f) in Eqs. T3 and T4] is given by

$$-2\mu\upsilon\left\langle \frac{\partial^2 u_i'}{\partial x_k \partial x_m}\frac{\partial^2 u_i'}{\partial x_k \partial x_m}\right\rangle \approx -\rho\upsilon^2\frac{u^2}{L^4} \approx -\rho\frac{L^4}{t_s^2}\frac{u^2}{L^4} \approx -C_{\varepsilon 2}\rho\frac{\varepsilon^2}{k}. \tag{10}$$

Table 1. Turbulence Model Details

Generalized ;transport equation
for k,ε and k_{sgs}: {accumulation} + {convection} = {production} + {turbulent tranport} + {viscous transport} + {dissipation}

Reynolds stress : {accumulation} + {convection} = {production} + {turbulent tranport} + {viscous transport} + {dissipation} + {pressure strain}
(a) (b) (c) (d) (e) (f) (g)

k-εModel
k equation

Exact

$$\left\{\rho\frac{\partial k}{\partial t}\right\}+\left\{\rho\langle u_k\rangle\frac{\partial k}{\partial x_k}\right\}=\left\{-\rho\left\langle u_i'u_j'\right\rangle\frac{\partial\langle u_i\rangle}{\partial x_k}\right\}+\left\{\frac{\partial}{\partial x_k}\left(-\langle p'u_k'\rangle-\frac{1}{2}\rho\langle u_i'u_i'u_k'\rangle\right)\right\}+\left\{\frac{\partial}{\partial x_k}\left(\mu\frac{\partial k}{\partial x_k}\right)\right\}+\{-\rho\varepsilon\} \tag{T1}$$
(a) (b) (c) (d) (e) (f)

Modeled

$$\left\{\rho\frac{\partial k}{\partial t}\right\}+\left\{\rho\langle u_k\rangle\frac{\partial k}{\partial x_k}\right\}=\left\{\tau_{ij}\frac{\partial\langle u_i\rangle}{\partial x_j}\right\}+\left\{\frac{\partial}{\partial x_k}\left(\frac{\mu_t}{\sigma_k}\frac{\partial k}{\partial x_k}\right)\right\}+\left\{\frac{\partial}{\partial x_k}\left(\mu\frac{\partial k}{\partial x_k}\right)\right\}+\{-\rho\varepsilon\} \tag{T2}$$
(a) (b) (c) (d) (e) (f)

ε equation

Exact

$$\left\{\rho\frac{\partial\varepsilon}{\partial t}\right\}+\left\{\rho\langle u_j\rangle\frac{\partial\varepsilon}{\partial x_j}\right\}=\left\{\begin{array}{l}-2\mu\left(\left\langle\frac{\partial u_i'}{\partial x_j}\frac{\partial u_k'}{\partial x_j}\right\rangle+\left\langle\frac{\partial u_j'}{\partial x_i}\frac{\partial u_j'}{\partial x_k}\right\rangle\right)\frac{\partial\langle u_i\rangle}{\partial x_k}\\-2\mu\left\langle u_k'\frac{\partial u_i'}{\partial x_j}\right\rangle\frac{\partial^2\langle u_i\rangle}{\partial x_k\partial x_j}-2\mu\left\langle\frac{\partial u_i'}{\partial x_k}\frac{\partial u_i'}{\partial x_m}\frac{\partial u_k'}{\partial x_m}\right\rangle\end{array}\right\}+\frac{\partial}{\partial x_j}\left\{\begin{array}{l}-\mu\left\langle u_j'\frac{\partial u_i'}{\partial x_m}\frac{\partial u_i'}{\partial x_m}\right\rangle\\-2\upsilon\left\langle\frac{\partial p'}{\partial x_m}\frac{\partial u_j'}{\partial x_m}\right\rangle\end{array}\right\}+\left\{\frac{\partial}{\partial x_j}\left(\mu\frac{\partial\varepsilon}{\partial x_j}\right)\right\}+\frac{\partial}{\partial x_j}\left\{-2\mu\upsilon\left\langle\frac{\partial^2u_i'}{\partial x_k\partial x_m}\frac{\partial^2u_i'}{\partial x_k\partial x_m}\right\rangle\right\} \tag{T3}$$
(a) (b) (c) (d) (e) (f)

Modeled

$$\left\{\rho\frac{\partial\varepsilon}{\partial t}\right\}+\left\{\rho\langle u_j\rangle\frac{\partial\varepsilon}{\partial x_j}\right\}=\left\{\rho C_{\varepsilon1}\frac{\varepsilon}{k}\tau_{ij}\frac{\partial\langle u_i\rangle}{\partial x_j}\right\}+\left\{\frac{\partial}{\partial x_j}\left(\frac{\mu_t}{\sigma_\varepsilon}\frac{\partial\varepsilon}{\partial x_j}\right)\right\}+\left\{\frac{\partial}{\partial x_j}\left(\mu\frac{\partial\varepsilon}{\partial x_j}\right)\right\}+\left\{-C_{\varepsilon2}\rho\frac{\varepsilon^2}{k}\right\} \tag{T4}$$
(a) (b) (c) (d) (e) (f)

Reynolds Stress Model
Reynolds stress equation

Exact

$$\left\{\rho\frac{\partial\tau_{ij}}{\partial t}\right\}+\left\{\rho\langle u_k\rangle\frac{\partial\tau_{ij}}{\partial x_k}\right\}=\left\{-\rho\left(\tau_{ik}\frac{\partial\langle u_j\rangle}{\partial x_k}+\tau_{jk}\frac{\partial\langle u_i\rangle}{\partial x_k}\right)\right\}+\frac{\partial}{\partial x_k}\left\{\begin{array}{l}-\rho\left\langle u_i'u_j'u_k'\right\rangle\\-\left(\left\langle p'u_i'p'u_i'\right\rangle\delta_{jk}+\left\langle p'u_j'\right\rangle\delta_{ik}\right)\end{array}\right\}+\left\{\frac{\partial}{\partial x_k}\left(\mu\frac{\partial\tau_{ij}}{\partial x_k}\right)\right\}+\left\{-2\mu\left\langle\frac{\partial u_i'}{\partial x_k}\frac{\partial u_j'}{\partial x_k}\right\rangle\right\}+\left\{\left\langle p'\left[\frac{\partial u_j'}{\partial x_i}+\frac{\partial u_i'}{\partial x_j}\right]\right\rangle\right\} \tag{T5}$$
(a) (b) (c) (d) (e) (f) (g)

(*Continued*)

Table 1. (Continued)

Generalized ;transport equation
for k,ε and k_{sgs}: {accumulation} + {convection} = {production} + {turbulent tranport} + {viscous transport} + {dissipation}

Reynolds stress : {accumulation} + {convection} = {production} + {turbulent tranport} + {viscous transport} + {dissipation} + {pressure strain}
(a) (b) (c) (d) (e) (f) (g)

Modeled

$$\left\{\rho\frac{\partial\tau_{ij}}{\partial t}\right\}+\left\{\rho\langle u_k\rangle\frac{\partial\tau_{ij}}{\partial x_k}\right\}=\left\{-\rho\left(\tau_{ik}\frac{\partial\langle u_j\rangle}{\partial x_k}+\tau_{jk}\frac{\partial\langle u_i\rangle}{\partial x_k}\right)\right\}+\left\{\frac{\partial}{\partial x_k}\left(\frac{\mu_t}{\sigma_k}\frac{\partial\tau_{ij}}{\partial x_k}\right)\right\}+\left\{\frac{\partial}{\partial x_k}\left(\mu\frac{\partial\tau_{ij}}{\partial x_k}\right)\right\}+\left\{-\frac{2}{3}\varepsilon\delta_{ij}\right\}+\{\Pi_{ij}\}\tag{T6}$$
(a) (b) (c) (d) (e) (f) (g)

ε equation

Exact

$$\left\{\rho\frac{\partial\varepsilon}{\partial t}\right\}+\left\{\rho\langle u_j\rangle\frac{\partial\varepsilon}{\partial x_j}\right\}=\left\{\begin{array}{l}-2\mu\left(\left\langle\frac{\partial u_i'}{\partial x_j}\frac{\partial u_k'}{\partial x_j}\right\rangle+\left\langle\frac{\partial u_j'}{\partial x_i}\frac{\partial u_j'}{\partial x_k}\right\rangle\right)\frac{\partial\langle u_i\rangle}{\partial x_k}\\-2\mu\left\langle u_k'\frac{\partial u_i'}{\partial x_j}\right\rangle\frac{\partial^2\langle u_i\rangle}{\partial x_k\partial x_j}-2\mu\left\langle\frac{\partial u_i'}{\partial x_k}\frac{\partial u_i'}{\partial x_m}\frac{\partial u_k'}{\partial x_m}\right\rangle\end{array}\right\}+\frac{\partial}{\partial x_j}\left\{\begin{array}{l}-\mu\left\langle u_j'\frac{\partial u_i'}{\partial x_m}\frac{\partial u_i'}{\partial x_m}\right\rangle\\-2\upsilon\left\langle\frac{\partial p'}{\partial x_m}\frac{\partial u_j'}{\partial x_m}\right\rangle\end{array}\right\}+\left\{\frac{\partial}{\partial x_j}\left(\mu\frac{\partial\varepsilon}{\partial x_j}\right)\right\}+\frac{\partial}{\partial x_j}\left\{-2\mu\upsilon\left\langle\frac{\partial^2u_i'}{\partial x_k\partial x_m}\frac{\partial^2u_i'}{\partial x_k\partial x_m}\right\rangle\right\}\tag{T7}$$
(a) (b) (c) (d) (e) (f)

Modeled

$$\left\{\rho\frac{\partial\varepsilon}{\partial t}\right\}+\left\{\rho\langle u_j\rangle\frac{\partial\varepsilon}{\partial x_j}\right\}=\left\{\rho C_{\varepsilon1}\frac{\varepsilon}{k}\tau_{ij}\frac{\partial\langle u_i\rangle}{\partial x_j}\right\}+\left\{\frac{\partial}{\partial x_j}\left(\frac{\mu_t}{\sigma_\varepsilon}\frac{\partial\varepsilon}{\partial x_j}\right)\right\}+\left\{\frac{\partial}{\partial x_j}\left(\mu\frac{\partial\varepsilon}{\partial x_j}\right)\right\}+\left\{-C_{\varepsilon2}\rho\frac{\varepsilon^2}{k}\right\}\tag{T8}$$
(a) (b) (c) (d) (e) (f)

Large eddy simulation
One-equation subgrid kinetic energy model

Exact

$$\left\{\rho\frac{\partial k_{sgs}}{\partial t}\right\}+\left\{\rho\overline{u}_k\frac{\partial k_{sgs}}{\partial x_k}\right\}=\left\{-\rho\overline{u_{i,sgs}u_{j,sgs}}\frac{\partial\overline{u}_i}{\partial x_k}\right\}+\left\{\frac{\partial}{\partial x_k}\left(\frac{-1}{2}\rho\overline{u_{i,sgs}u_{i,sgs}u_{k,sgs}}-\overline{p_{sgs}u_{k,sgs}}\right)\right\}+\frac{\partial}{\partial x_k}\left\{\mu\frac{\partial k_{sgs}}{\partial x_k}\right\}+\{-\rho\varepsilon_{sgs}\}\tag{T9}$$
(a) (b) (c) (d) (e) (f)

Modeled

$$\left\{\rho\frac{\partial k_{sgs}}{\partial t}\right\}+\left\{\rho\overline{u}_k\frac{\partial k_{sgs}}{\partial x_k}\right\}=\left\{\overline{\tau}_{ik}\frac{\partial\overline{u}_i}{\partial x_k}\right\}+\left\{\frac{\partial}{\partial x_k}\frac{\mu_{sgs}}{\sigma_k}\frac{\partial k}{\partial x_k}\right\}+\frac{\partial}{\partial x_k}\left\{\mu\frac{\partial k_{sgs}}{\partial x_k}\right\}+\left\{-C_\varepsilon\rho\frac{k_{sgs}^{3/2}}{\Delta}\right\}\tag{T10}$$
(a) (b) (c) (d) (e) (f)

The abovementioned modeling of k and ε equations result into five turbulence parameters C_μ, $C_{\varepsilon 1}$, $C_{\varepsilon 2}$, σ_k and σ_ε. These parameters have been estimated from studies in simple flows. In the log-law region of the boundary layer, experimentally it has been found that the turbulence production and the dissipation terms are much larger than the other terms. Turbulence in this region is considered to be in local equilibrium. Neglecting transport and production in this flow, value of $C_\mu = 0.09$ has been obtained. For the value of $C_{\varepsilon 2}$, experiments have been carried out in decaying grid turbulence. Turbulence is generated when free flow goes through a grid that generates mean flow gradients and in turn via the production term generates turbulence. Sufficiently far downstream, the velocity gradients are zero, and hence the production and dissipation terms are zero in contrast to log-law region in the boundary layer. The turbulent diffusion term is also negligible. The balance of turbulence convection and dissipation gives $C_{\varepsilon 2} = 1.92$. The constant $C_{\varepsilon 1}$ is obtained by looking at the dissipation rate equation in the log-region of boundary layer. The turbulent diffusion is not negligible in this case unlike k equation. The simplifications of ε equation using velocity profiles in log-law region and the numerical solution of these equations give $C_{\varepsilon 1} = 1.44$, σ_k and $\sigma_\varepsilon = 1.0$ and 1.3, respectively.

The standard k-ε model has performed satisfactorily in many flows, but the applicability of this model is limited due to uncertainties involved in the modeling of turbulence production, turbulent transport, and the assumptions in modeling dissipation rate equation [terms (c) and (d) in Eqs. T1–T4]. Furthermore, the modeling of transport equations for k and ε pose the difficulties to account for streamline curvature, rotational strains, and the other body-force effects. This particular fact led to the development of RSM.

In the case of RSM, rather than modeling the turbulence production, all the six stress equations (Eq. T5, Table 1) are solved and ε equation (Eq. T7, Table 1) is kept the same as in the standard k-ε model (Eqs. T3 and T4, Table 1). The major difference between modeling k-equation and Reynolds stress equation is (a) turbulence production term and (b) energy redistribution term (i.e. pressure strain term; Eqs. T2 and T6, Table 1). The similarity in k-ε model and RSM is (a) modeling of turbulent transport using gradient diffusion hypothesis (b) modeling of ε equation. Modeling of terms in Reynolds stress equation is discussed below.

The modeled turbulent diffusion term [term (d) in Eqs. T5 and T6] is given by:

$$\frac{\partial}{\partial x_k}\left[\rho\left\langle u_i' u_j' u_k'\right\rangle + \left(\left\langle \mathrm{P}' u_i'\right\rangle \delta_{jk} + \left\langle \mathrm{P}' u_j'\right\rangle \delta_{ik}\right)\right] = \frac{\partial}{\partial x_k}\left(\frac{\mu_t}{\sigma_k}\frac{\partial \tau_{ij}}{\partial x_k}\right). \tag{11}$$

The pressure strain term is the most uncertain term in the RSM. This term is responsible for making turbulence isotropic and redistribution of energy between components $\langle u_1'^2\rangle, \langle u_2'^2\rangle$, and $\langle u_3'^2\rangle$. The incompressibility condition guarantees that $\Pi_{11} + \Pi_{22} + \Pi_{33} = 0$. If individual terms of Π_{ii} are nonzero, at least one must be positive and one negative. The classical approach is to decompose pressure strain term in slow part, rapid part, and wall-reflection term.

The pressure strain term [term (g) in Eqs. T5 and T6] in Table 1 is modeled as (Launder[25]):

$$\Pi_{ij} = \left\langle p'\left[\frac{\partial u_j'}{\partial x_i} + \frac{\partial u_i'}{\partial x_j}\right]\right\rangle = \Pi_{ij,\mathrm{slow}} + \Pi_{ij,\mathrm{rapid}} + \Pi_{ij,\mathrm{wall}}, \tag{12}$$

$$\Pi_{ij,\mathrm{slow}} = -C_1 \rho \frac{\varepsilon}{k}\left[\left\langle u_i' u_j'\right\rangle - 2\delta_{ij}k\right], \tag{13}$$

$$\Pi_{ij,\mathrm{rapid}} = -C_2\left[\left(P_{ij} - C_{ij}\right) - 2\delta_{ij}(P + C)\right], \tag{14}$$

$$\left.\begin{aligned} P_{ij} &= -\rho\left\langle u_i' u_j'\right\rangle \tfrac{\partial \langle u_i\rangle}{\partial x_k}, \quad P = 0.5P_{kk} \\ C_{ij} &= \rho\langle u_k\rangle \tfrac{\partial \langle u_i' u_j'\rangle}{\partial x_k}, \quad C = 0.5C_{kk} \end{aligned}\right\} \tag{15}$$

$$\Pi_{ij,\mathrm{wall}} = C_{w,1}\frac{\varepsilon}{k}\left(\langle u_k' u_m'\rangle n_k n_m \delta_{ij} - \frac{3}{2}\langle u_i' u_k'\rangle n_j n_k - \frac{3}{2}\langle u_i' u_k'\rangle n_i n_k\right)\frac{k^{3/2}}{C_l \varepsilon d} + C_{w,2}\frac{\varepsilon}{k}\left(\Pi_{km,\mathrm{rapid}} n_k n_m \delta_{ij} - \frac{3}{2}\Pi_{ik,\mathrm{rapid}} n_j n_k - \frac{3}{2}\Pi_{jk,\mathrm{rapid}} n_i n_k\right)\frac{k^{3/2}}{C_l \varepsilon d}. \tag{16}$$

The slow and rapid parts (Eqs. 13–15) redistribute velocity fluctuations in the "free flow." When the flow approaches wall, the velocity components are influenced by solid surface and turbulence need not be isotropic anymore and wall reflection term (Eq. 16) plays a dominant role. This term redistributes normal stresses near the wall.

Dissipation is assumed to be isotropic and the modeled dissipation term [term (f) in Eqs. T5 and T6] is given by:

$$2\mu\left\langle \frac{\partial u_i'}{\partial x_k}\frac{\partial u_j'}{\partial x_k}\right\rangle = \varepsilon_{ij} = \frac{2}{3}\varepsilon\delta_{ij}. \tag{17}$$

LES has a very different approach in terms of turbulence modeling. In LES, the transport equations are derived by applying a space filtering operation to Eqs. 1 and 2. The filtering process effectively filters out eddies whose scales are smaller than the filter width or grid spacing used in the meshing. The resulting equations are as follows:

$$\frac{\partial \bar{u}_i}{\partial x_i} = 0, \tag{18}$$

$$\rho\frac{\partial \bar{u}_i}{\partial t} + \rho\bar{u}_j\frac{\partial \bar{u}_i}{\partial x_j} = -\frac{\partial \bar{p}}{\partial x_i} + \frac{\partial}{\partial x_j}\left(\mu\frac{\partial \bar{u}_i}{\partial x_j} - \rho\overline{u_{i,\mathrm{sgs}}u_{j,\mathrm{sgs}}}\right). \tag{19}$$

It can be seen that the equations have the structure as the original equation (Eq. 2) plus additional terms, called subgrid scale stresses (SGS).

In LES, SGS modeling is done as follows:

$$-\rho\overline{u_{i,\mathrm{sgs}}u_{j,\mathrm{sgs}}} = \overline{\tau}_{ij} = \frac{2}{3}\rho k_{\mathrm{sgs}}\delta_{ij} - \mu_{\mathrm{sgs}}\left(\frac{\partial \bar{u}_i}{\partial x_j} + \frac{\partial \bar{u}_j}{\partial x_i}\right). \tag{20}$$

Similar to ensemble-averaging approach, μ_{sgs} is estimated from zero equation model (Smagorinsky model), one equation model (SGS kinetic energy equation), etc. In one equation model, μ_{sgs} is estimated from the one equation subgrid scale kinetic energy model[26] and is given by:

$$\mu_{sgs} = C_d \Delta \rho k_{sgs}^{1/2}. \quad (21)$$

The exact and modeled transport equations for subgrid scale energy are reported in Table 1 (Eqs. T9 and T10, respectively). In LES, as the filter width is expected well within inertial subrange, local rate of dissipation is estimated from the transfer of energy from one scale to next. The formulation for ε_{sgs} is given as (Eq. T10):

$$\varepsilon_{SGS} = \overline{\tau}_{ij}\overline{S}_{ij}\overline{S}_{ij} = -C_\varepsilon \frac{k_{sgs}^{3/2}}{\Delta}. \quad (22)$$

With this brief background of turbulence modeling, a discussion on application of these models to jets in the literature is presented in the next section. Comments have been made regarding the validity of assumptions in k-ε model using RSM and LES in results and discussion section.

Previous work on computational modeling of jets

As regards to JLR, the previous work[9–20] has been critically reviewed by Jayanti[22] and Patwardhan.[23] These authors[22,23] have studied the mixing process in JLR over a wide variety of conditions like jet angle, jet velocity, jet diameter, reactor size, physical properties of fluid, etc. The results of these works had helped to develop empirical correlations and improve their reliability and accuracy to some extent. However, the majority of the published work in terms of detailed flow patterns is confined to axi-symmetric round jets and has been reviewed by Pope[6] and Hussein.[7] Hence, the desired understanding of detailed flow pattern in JLR (experimentally and computational) is still inadequate.

The standard k-ε model has been found to perform well for the plane jets, whereas for round jets overpredictions were observed in spreading rate (40%) and turbulent quantities.[27] Several modifications[27–31] have been proposed in the model constants of standard k-ε model to become applicable for turbulent round jets. The literature[27–31] pertaining to these studies is provided in Table 2. In these studies, the model parameter $C_{\varepsilon 1}$ and/or $C_{\varepsilon 2}$ has been taken as some function of the gradient of centerline velocity and $r_{1/2}$ (Launder et al.,[28] McGuirk and Rodi,[29] Morse,[30] and Rodi[31]), or C_μ in some cases (Patwardhan[23] and Basara and Jakirlić[32]). Pope[27] proposed additional constant $C_{\varepsilon 3}$ in the energy dissipation rate equation. He attempted to generalize the standard k-ε model by maintaining the conventional parameters and suggested the source of dissipation to be an increasing function of normalized invariance (χ). The LESs were performed by Lui et al.[33] and Ilyusin and Kranksky.[34] Lui et al.[33] developed a relationship between Leonard stresses and a nonlinear similarity subgrid-scale model to control the amount of kinetic energy backscatter. Ilyusin and Kranksky[34] used Smagorinsky model with different values of $C_S = 0.15$, 0.17, 0.19, and 0.21. They observed that the length of the initial region of a jet was strongly dependent on the value of Smagorinsky constant (C_S). Decreasing C_S value resulted into decreased length of initial region, and vice a versa. Finally, they recommended $C_S = 0.17$ that provided the best match of LES results to experimental data observed for the initial region. However, these LES studies were mainly

Table 2. Parametric Sensitivity Analysis for k-ε Model

SN	Model	Correlation	Model Constants (Literature)	Model Constants' Range	Optimum Model Constants	Constraint for Model Parameter	Performance of Modified Model
1	Standard k-ε model[24]	$C_\mu = 0.09$ $C_{\varepsilon 1} = 1.44$ $C_{\varepsilon 2} = 1.92$		$C_\mu = 0.04$–0.14 $C_{\varepsilon 1} = 1.36$–1.6 $C_{\varepsilon 2} = 1.8$–2.1			Deviations observed (Figure 5)
2	Rodi[31]	$C_\mu = 0.09\text{-}A_{f\mu}f$; $C_{\varepsilon 2} = 1.92\text{-}A_{f2}f$ $f = \left\lvert \frac{\delta_j}{\Delta\langle u_2\rangle} \left(\frac{\partial\langle u_{2,\varepsilon}\rangle}{\partial x_2} - \left\lvert \frac{\partial\langle u_{2,\varepsilon}\rangle}{\partial x_2} \right\rvert \right) \right\rvert^{e_f}$	$A_{f\mu} = 0.04$ $A_{f2} = 0.0667$ $e_f = 0.2$	$A_{f\mu} = 0.066$–0.15 $A_{f2} = 0.008$–0.06 $e_f = 0.2$–0.5	$A_{f\mu} = 0.02$ $A_{f2} = 0.008$ $e_f = 0.2$	$C_\mu = 0.04$ $C_{\varepsilon 1} = 0.04$	Deviations observed (Figure 5)
3	McGuirk and Rodi[29]	$C_{\varepsilon 1} = A_1 - A_2 \left\{ \frac{r_{1/2}}{\langle u_{2,\varepsilon}\rangle} \frac{d\langle u_{2,\varepsilon}\rangle}{dx_2} \right\}$	$A_1 = 1.14$ $A_2 = 5.31$	$A_2 = 0.05$–5.31 $A_1 = 0.9$–1.3	$A_1 = 1.14$ $A_2 = 0.1$	$C_{\varepsilon 1} \leq 2.0$	Deviations observed (Figure 5)
4	Morse[30]	$C_{\varepsilon 1} = 1.4 - A_1 \left\{ \frac{k}{\varepsilon} \frac{d\langle u_{2,\varepsilon}\rangle}{dx_2} \right\}^{e_1}_{\not<}$	$A_1 = 3.4$ $e_1 = 3$	$A_2 = 0.1$–5.4 $e_1 = 2$–4	$A_1 = 0.1$ $e_1 = 3$	$C_{\varepsilon 1} \leq 2.0$	Deviations observed (Figure 5)
5	Pope[27]	$\frac{D\varepsilon}{Dt} = \frac{\partial}{\partial x_j}\left(\upsilon + \frac{\upsilon_t}{\sigma_\varepsilon}\right)\frac{\partial\varepsilon}{\partial x_j} + \frac{\varepsilon^2}{k}\left(C_{\varepsilon 1}\frac{\mathcal{P}}{\varepsilon} - C_{\varepsilon 2} + C_{\varepsilon 3}\chi^{e_1}\right)$ $\chi = \omega_{ij}\omega_{jk}S_{ki}$ and $e_1 = 1$	$C_{\varepsilon 3} = 0.79$ $e_1 = 1$	$C_{\varepsilon 3} = 0.5$–80 $e_1 = 1$–1.5	$C_{\varepsilon 3} = 20$		Closer to experimental (Figure 6)
6	Hybrid model (Present)	$\frac{D\varepsilon}{Dt} = \frac{\partial}{\partial x_i}\left(\upsilon + \frac{\upsilon_t}{\sigma_\varepsilon}\right)\frac{\partial\varepsilon}{\partial x_i} + \frac{\varepsilon^2}{k}\left(C_{\varepsilon 1}\frac{\mathcal{P}}{\varepsilon} - C_{\varepsilon 2} + C_{\varepsilon 3}\chi\right)$ $\chi = \omega_{ij}\omega_{jk}S_{ki}$		$C_{\varepsilon 3} = 1$–8	$C_{\varepsilon 3} = 2$	$C_\mu = \frac{-\langle u_i u_j\rangle \frac{\partial\langle u_i\rangle}{\partial x_j}}{\frac{\varepsilon^2}{\varepsilon}\lvert S_{ij}\rvert^2}$	Good agreement with experimental and best amongst above (Figure 6)

limited to subgrid scale modeling rather than in depth knowledge of transient turbulent flow structures and gaining the insight into limitations of RANS models.

On the basis of the analysis of the previous work, it was thought desirable to undertake a systematic experimental and computational investigation of JLR. In particular

1. Most of the literature deals with free jet simulation, whereas flow in JLR is expected to be different than free jets. LES simulations have been used to quantify these differences.

2. To find suitability of different turbulence models for JLR, extensive PIV measurements have been carried out for the validation of simulation results.

3. The variants of k-ε model suggested for the round jets[27–31] (listed in Table 2) have been used to study the flow in JLR and also sensitivity analysis of model parameter has also been carried out. To test the assumptions in modeling production and transport terms in k-ε model, simulations have been carried out using the RSM and LES models. A hybrid model (combination of Pope[27] and Basara and Jakirlić[32] models) has been developed, which improved the predictions to a great extent.

4. It is generally believed that, at the same power consumption, the flow in JLR creates more convection when compared with that in stirred tank reactors (STRs). To understand the physics behind these observations, we have compared the values of average liquid circulation velocity (V_C) and k in JLR and STR provided with a hydrofoil impeller (which is supposed to produce relatively very high convective motion among those produced by various impeller designs). Furthermore, suitability of the hybrid k-ε model [in objective (3) above] has been examined for the predictions of flow in stirred vessels.

5. Mixing time studies have been undertaken in JLR and STR at the same power consumption and for different nozzle diameters.

Experimental

The measurements were performed in a cylindrical plexiglass tank of 0.3-m internal diameter and 0.4-m height. The liquid was circulated using an external 0.5 HP centrifugal pump. The nozzle position was fixed at $H_N/D = 1$ with downward orientation (Figure 1). The experiments were conducted for the nozzle diameter of 20 mm for the flow rate of 0.542 kg/s. The cylindrical tank was enclosed in another tank of square cross-section and the space between the two was filled with water to minimize the refraction effects. For the measurement of flow, PIV was used. The PIV technique consisted of a pulsed dual Nd:YAG laser from TSI having pulse duration of 6 ns and was synchronized with the camera using synchronizer. Optics included a combination of cylindrical and spherical lenses, attached in view of creating a thin laser sheet of 1-mm thickness. A high-resolution 4M CCD camera (Powerview plus, TSI) of 15 Hz frequency was placed at right angle to the laser sheet. A zoom lens (AF micro Nikkor, 60 mm) from Nikon was used for capturing the window size of 45 mm $\times$ 45 mm. The images were recorded with resolution of 2048 $\times$ 2048 pixels. The flow was seeded with hollow glass-silver beads of 20-μm diameter and 1050 kg/m^3 making sure that the Stokes number for the measurement be small enough for particles to follow the path of the fluid. The recorded images were divided into interrogation area of 64 $\times$ 64 pixels with a 50% overlap, resulting in approximately 4000 vectors for the image. Thus, a vector spacing of 0.750 mm was obtained. The time difference between the two laser pulses was optimized based on Nyquist criterion. A nonlinear calibration analysis was carried out to obtain accurate values of the velocities.

PIV data processing and estimation of turbulent kinetic energy dissipation rate

PIV data were further processed to eliminate the spurious vectors. The data were first subjected to the high and low pass filters to eliminate out-of-range vectors. Furthermore, the data were double correlated to find the relative direction of neighboring vectors and thus deciding the flow governing vectors and removing the noise. The processed data were used further for the calculation of mean and turbulence quantities. The turbulent dissipation rate (ε) was estimated using the algorithm based on third-order structure function as suggested by Pope,[6] Lindborg,[35] and Kang et al.[36] who applied it for multiple probe hot film anemometer (HFA). This method has been considered mainly because the measurement vector spacing ($\sim$0.750 mm) has been found to be about 20 times more than the Kolmogorov length scale (η), the dissipation scale is not sufficiently resolved in the present experiments. Therefore, ε cannot be obtained accurately from the derivative variance. The procedure has been extended for PIV as described below. Second- and third-order structure functions can be obtained as:

$$D_{\mathrm{uu}} = \left\langle [(u_2(x_2 + r_{\mathrm{D}}) - u_2(x_2))]^2 \right\rangle, \tag{23}$$

$$D_{\mathrm{uuu}} = \left\langle [(u_2(x_2 + r_{\mathrm{D}}) - u_2(x_2))]^3 \right\rangle, \tag{24}$$

whereas, the relationship between D_{uuu} and ε can be obtained as:

$$D_{\mathrm{uuu}} = -\frac{4}{5}\varepsilon r_{\mathrm{D}} + 6\upsilon\frac{\partial D_{\mathrm{uu}}}{\partial r_{\mathrm{D}}} - \frac{3}{r_{\mathrm{D}}^4}\int_0^r r'_D 4\frac{\partial D_{\mathrm{uu}}}{\partial t}\, dr'_{\mathrm{D}}. \tag{25}$$

The second term on the right-hand side of Eq. 25 shows the effect of diffusivity whereas the last term represents the decay in the mean flow direction. The Eq. 25 assumes homogeneous turbulence, and, hence, it is applicable only locally on a small length scale. In the present study, the maximal value of the separation distance, r_{D}, was 4 mm and integral length scale ($k^{3/2}/\varepsilon$) was 12 mm. These two length scales support the validity of homogeneity assumption. To calculate $\frac{\partial D_{\mathrm{uu}}}{\partial t}$ in Eq. 25, Kolmogorov's second similarity hypothesis ($D_{\mathrm{uu}} = C\varepsilon^{2/3}r_{\mathrm{D}}^{2/3}$) and the k-ε model for the decay of the dissipation ($\frac{\partial \varepsilon}{\partial t} = -C_{\varepsilon 2}\frac{\varepsilon^2}{k}$) were used. Thus, Eq. 25 becomes:

$$\frac{D_{\mathrm{uuu}}}{\varepsilon r_{\mathrm{D}}} = -\frac{4}{5} + C\left[4\left(\frac{r_{\mathrm{D}}}{\eta}\right)^{-4/3} + \frac{2\sqrt{2}C_{\varepsilon 2}}{\sqrt{5}}\frac{\upsilon}{k\lambda}\left(\frac{r_{\mathrm{D}}}{\eta}\right)^{2/3}\right]. \tag{26}$$

The third-order structure functions were evaluated using PIV data for the substitution in Eq. 23. The values of ε in Eq. 26 have been determined by iterative process. The unknown parameters, namely, C, $C_{\varepsilon 2}$ have been set to 1.7

and 2, respectively. The details regarding the optimization of these parameters have been discussed elsewhere.[37]

CFD Simulations

Turbulence models and method of solutions

Standard k-ε Model and RSM. In case of standard k-ε model and RSM simulations, QUICK discretization scheme has been used for momentum and turbulence equations, whereas second-order accurate PISO algorithm has been used for pressure-velocity coupling in momentum equation. The simulations have been carried out in Fluent 6.2 with standard model parameters. In case of RSM, shear stress transport model has been used. The hexahedral grids with 0.6 million node points were used for simulation using k-ε model and RSM.

LES Model. In case of LES modeling, dynamic Smagorinsky subgrid scale (SGS) model has been used for closure in Fluent 6.2. In this model, model coefficient was calculated dynamically at every time step based on Leonard stress. The hexahedral grid was taken and 2.5 million node points were used. The fluctuations have been artificially given to the inlet profile by random number generation program. The details of model equations are given in Table 1. The simulations have been performed with a staggered grid arrangement and with bounded central difference discretization scheme for momentum. For pressure-velocity coupling, PISO scheme was used. The second-order implicit time discretization has been adapted with time increment of 5×10^{-4} sec.

Boundary conditions

In the present case, two computational domains were considered, one for simulating flow inside the nozzle and other for simulating the flow in JLR (which is our domain of interest). The simulation of flow inside the nozzle was necessary for setting exact inlet boundary condition for other domain. The velocity profiles at the outlet of nozzle were taken as the inlet velocity for JLR. The velocity at the outlet of JLR was fed directly to the inlet of nozzle. The pump and recycle pipes are neglected in CFD simulations. The tank walls and the base of the tank were specified as impermeable boundaries. Thus, velocity component normal to the surface is set to zero. The top liquid surface was simulated as a flat interface. The normal flux and the gradients of the other quantities were specified to be zero.

Results and Discussion

Comparison of JLR with turbulent round jet

It is known that the turbulent round jets[6,7] exhibit self-similar profiles when scaled with centerline velocity and $r_{1/2}$. Therefore, it was thought desirable to examine the flow in JLR for self-similarity using LES. Figure 2A shows the mean axial velocity against the radial distance in JLR at three different axial locations. It can be observed that all the profiles tend to fall on single curve for axial velocity, whereas the radial velocities do not follow self-similar pattern (Figure 2B). In the case of round jets, both profiles fall on a single curve exhibiting self-similarity. Furthermore, the round jet spreads linearly and the spreading rate is almost constant ($\sim$0.096) showing very weak dependence on Reynolds number (Pope[6]). In the case of JLR, the jet spreading is not linear (Figure 2C) and the spreading rate was observed to vary from 0.098 to 0.213. Figure 2D shows the profiles of Reynolds stresses in JLR. The results are order of magnitude higher for JLR compared with the experimental results in round jets.[7] The $\langle u_1' u_2' \rangle$ stress was observed to be very small compared with the normal stresses in JLR. These evidences clearly suggest nonself similar flows in JLR.

Comparison between various turbulence models and the experimental PIV data

The simulations have been performed using standard k-ε model, RSM, and LES. The predictions of the profiles of mean velocity (axial and radial), turbulent kinetic energy and turbulent energy dissipation rate have been compared with the experimental data. The quantitative comparison has been presented at two axial locations, $x_2 = 0.1$ and 0.2 m from the bottom (Figure 1). The deviations have been expressed in terms of mean error.

Figure 3 shows the comparison for radial profile of axial velocity in JLR. The axial flow (Figure 3A and 3B) was distinctly downward in the central region with very high velocities, whereas an upward counter flow was observed in the near wall region. The point of flow reversal was clearly seen at a radial location (x_1) of around 0.1 m, whereas it was shifted closer to central axis as one move close to the nozzle (Figures 3A and B). At $x_2 = 0.2$ m (Figure 3A), in the central region, k-ε model predictions showed satisfactory agreement with experimental values (24%), whereas RSM (12%) and LES (9%) showed good agreement. As the flow approaches bottom wall ($x_2 = 0.1$, Figure 3B), LES, RSM showed excellent agreement (deviation 4% and 6%, respectively) with the experiments, whereas standard k-ε model was found to deviate by 13%.

Figures 3C and D show the comparison of the radial profiles of radial velocity. The experimental observation shows steep inward value in the high shear zone (negative radial velocity) and outward radial velocity in the jet zone (positive radial velocity). The fluid from surrounding stagnant pool was entrained in the central region because of the high shear (velocity gradients) generated by high velocity fluid from nozzle. These phenomena create circulation currents in JLR. At $x_2 = 0.2$ m (Figure 3C), in all three models, the results showed very poor agreement (k-ε model, 91%, RSM, 65% and LES 33%). Between $0.03 < x_1 < 0.12$ m, LES was in very good agreement with experimental data. At $x_2 = 0.1$ m (Figure 3D), standard k-ε model showed large deviation (98%) from the experimental observation. However, LES and RSM follow the trend of experimental values till $x_1 = 0.04$ m and after that showed deviation (RSM, 36%, LES, 29%) as compared with the experiments.

Turbulent kinetic energy, calculated from the PIV experiments and that predicted from simulations have been plotted in Figure 4A and B. The turbulent kinetic energy shows a peak in central region. At the location, $x_2 = 0.2$ m (Figure 4A) all the three models were found to predict close to the experimental data till $x_1 = 0.1$ m and farther towards the wall they were found to underpredict (k-ε model, 40%, RSM, 28%, and LES, 22%). Furthermore, at $x_2 = 0.1$ m

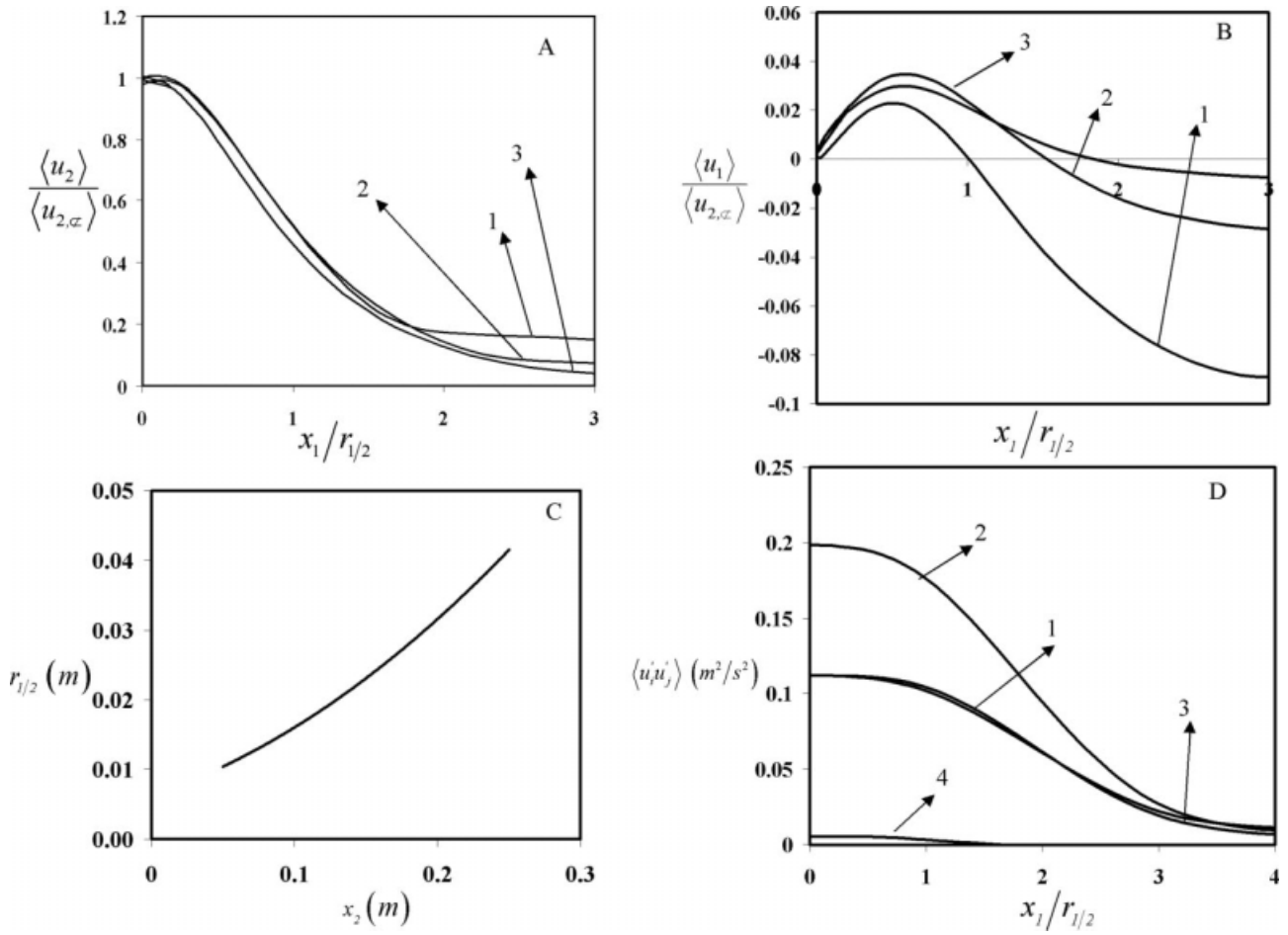

Figure 2. Comparison of JLR with turbulent round jet.

(A) Axial velocity profile, (B) radial velocity profile 1 $x_2 = 0.28$ m; 2 $x_2 = 0.2$ m; 3 $x_2 = 0.1$ m, (C) variation of $r_{1/2}$ with axial distance, and (D) Reynolds stress profile at $x_2 = 0.2$ m, 1 $\langle u_1 u_1 \rangle$, 2 $\langle u_2 u_2 \rangle$, 3 $\langle u_3 u_3 \rangle$ and 4 $\langle u_1 u_2 \rangle$.

(Figure 4B), k-ε model, RSM, and LES were in good agreement from center to $x_1 = 0.04$ m, whereas in the bulk region till $x_1 = 0.13$ m, standard k-ε model and LES were found to overpredict (45% and 38%, respectively) and RSM underpredict (42%) the experimental values.

The comparison of turbulent dissipation rate has been shown in Figures 4C and D. Maximum dissipation rate is observed in the central region and it follows the trend of k as shown in Figures 4A and B. All the models showed qualitative and quantitative trend which are the same as those of experimental results. At $x_2 = 0.2$ (Figure 4C), the predictions using RSM were improved (19% deviation). At $x_2 = 0.1$ m (Figure 4D), the deviations for k-ε model, RSM and LES were 27%, 21% and 19%, respectively.

This discussion clearly brings out that the k-ε model in its standard form fails to predict the flow accurately. Similar observations have been reported for round jets in the literature.[27–31] Many modifications have been suggested to the standard k-ε model using different values for model parameters, as a function of centerline velocity and $r_{1/2}$, addition of one more constant, etc. Next section deals with the application and assessment of such modifications for the case of JLR.

Parametric sensitivity of the k-ε models

This section deals with the investigation of the sensitivity of k-ε model parameters on the flow patterns in JLR using the modifications suggested in the literature for round jets. Any such modification with consistent and reliable results would be of great help for the design engineers as the k-ε models are computationally attractive for the simulation of large scale equipment in chemical process industry.

A large number of recommendations have been proposed in the literature for the estimation of model parameters (C_μ, $C_{\varepsilon 1}$, and $C_{\varepsilon 2}$). These have been summarized in Table 2. In the table, column 2 shows the model correlations in terms of model constants as proposed in the literature. Column 3 shows the values of the model constants as reported in the literature. Column 4 represents the range over which these model constants have been varied to study the sensitivity in the present study. Column 5 and 6 represent the optimum values of these constants for the present case and constraint put over these parameters during the simulations. Column 7 describes the remarks based on the performance of each of the model for the present case. A procedure for each of the model is as follows:

1. The various models discussed in this work, as reported in Table 2, have variation of parameters in axial and radial

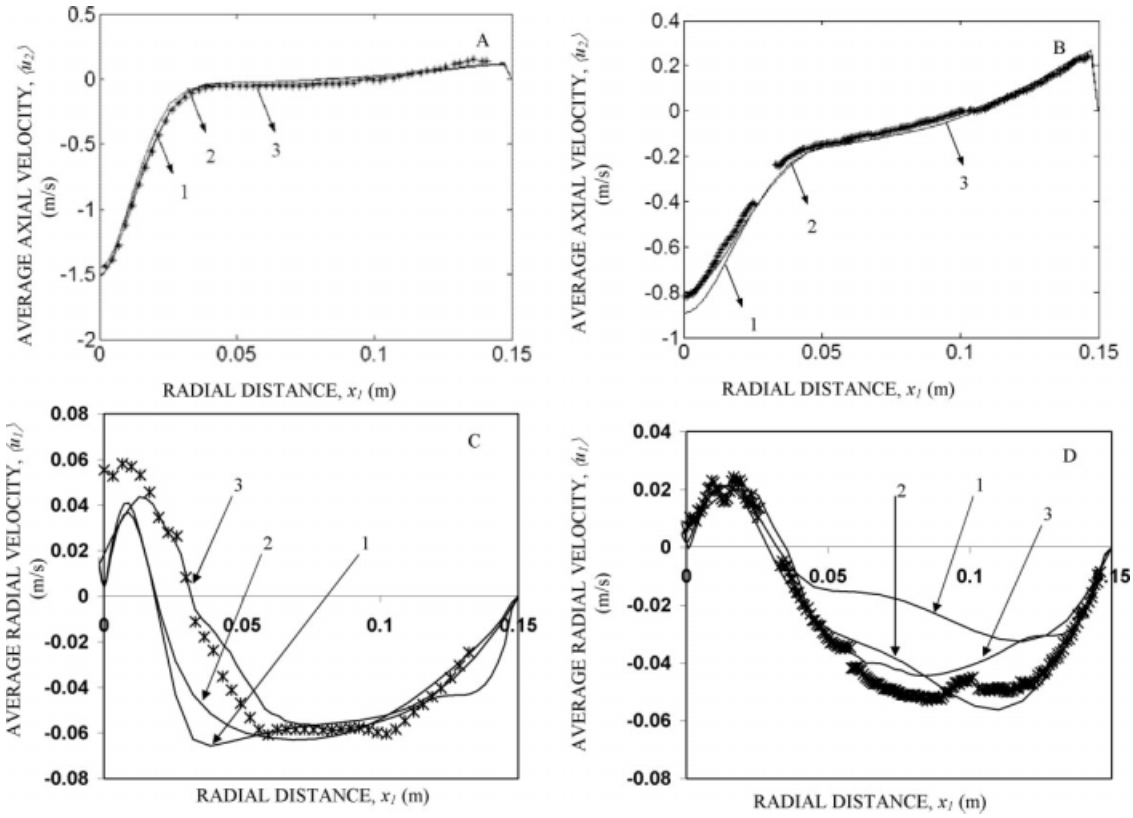

Figure 3. Radial profiles of mean velocity for flow rate of 0.542 kg/s.

(A) Radial profiles of axial velocity at $x_2 = 0.2$ m; (B) Radial profiles of axial velocity $x_2 = 0.1$ m; (C) Radial profiles of radial velocity at $x_2 = 0.2$ m; and (D) Radial profiles of radial velocity $x_2 = 0.1$ m: 1 k-ε model; 2 RSM; and 3 LES model; *PIV Results.

direction. After solving these model equations, at each location (in axial and radial direction) values of $C_\mu, C_{\varepsilon 1}$, and $C_{\varepsilon 2}$ were different than standard values. These values were dependent on various parameters (A_1, A_2, e_1, etc.) in the models. Based on the variation of these parameters, deviation in mean flow, and turbulence properties has been checked.

2. The check on validity of the model has been performed in the following order: i.e. first axial velocity profile, then radial velocity profile, followed by turbulent kinetic energy and then the energy dissipation rate. For example, if a model parameter shows satisfactory agreement for axial velocity profile and significant deviations for radial velocity profile, then the comparison for k and $\boldsymbol{\varepsilon}$ was not undertaken. This is because, if any improvement fails to predict the mean flow, then it is unlikely to predict correctly the turbulence quantities. In such cases, the next sets of parameters were selected.

3. The various models, as reported in Table 2, have variation of constants $C_\mu, C_{\varepsilon 1}$, and $C_{\varepsilon 2}$ in axial and radial direction. After solving these model equations, at each location (in axial and radial direction) values of $C_\mu, C_{\varepsilon 1}$, and $C_{\varepsilon 2}$ were different than standard k-ε model values. These values were dependent on various parameters in the models. An attempt has been made to tune these model parameters in order to get good agreement with the experimental data.

To evaluate the parametric sensitivity of standard k-ε model, model parameters such as C_μ ($0.04 < C_\mu < 0.14$), $C_{\varepsilon 1}$ ($1.3 < C_{\varepsilon 1} < 1.6$), $C_{\varepsilon 2}$ ($1.8 < C_{\varepsilon 2} < 2.1$) have been varied independently to estimate the effect on mean velocities and turbulence parameters. Figures 5A and B show the results for each of the parameter value at $x_2 = 0.1$ m. It can be observed (Figure 5A) that for $C_{\varepsilon 1} = 1.3$ and $C_\mu = 0.135$ (line 8) axial velocity spread is found to be higher, while magnitude in the centerline has been lesser than the experimental observation. Only two of the modifications of model parameters ($C_\mu = 0.05$; line 4) have improved the predictions of axial velocity. Minimum deviation was observed with $C_{\varepsilon 2} = 2.1$ (line 5; 13%) and maximum with $C_m = 0.135$ (line 6; 28%). For $C_{\varepsilon 2} = 1.8$ and $C_\mu = 0.05$ (line 3 and line 4, respectively), the value of axial velocity has been overpredicted and the radial spread of axial velocity was found to be steeper. However, it can be seen that all these modifications (except RSM) failed very close to centerline. Similarly, for radial velocity profiles also (Figure 5B), the location of maxima was found to be shifted indicating larger spread than that observed experimentally. All these modifications (% deviation $\sim$ 160%) have failed to predict the radial velocity profile compared with the standard k-ε model (% deviation = 98%). Figures 5A and B show that any combinations of model parameter values do not provide improved agreement with the experimental data, so the further analysis for turbulence quantities is not reported here.

In view of this, the study has been extended further to evaluate the effectiveness of modified k-ε model.[27,29–31] The two-dimensional modified k-ε models available in the

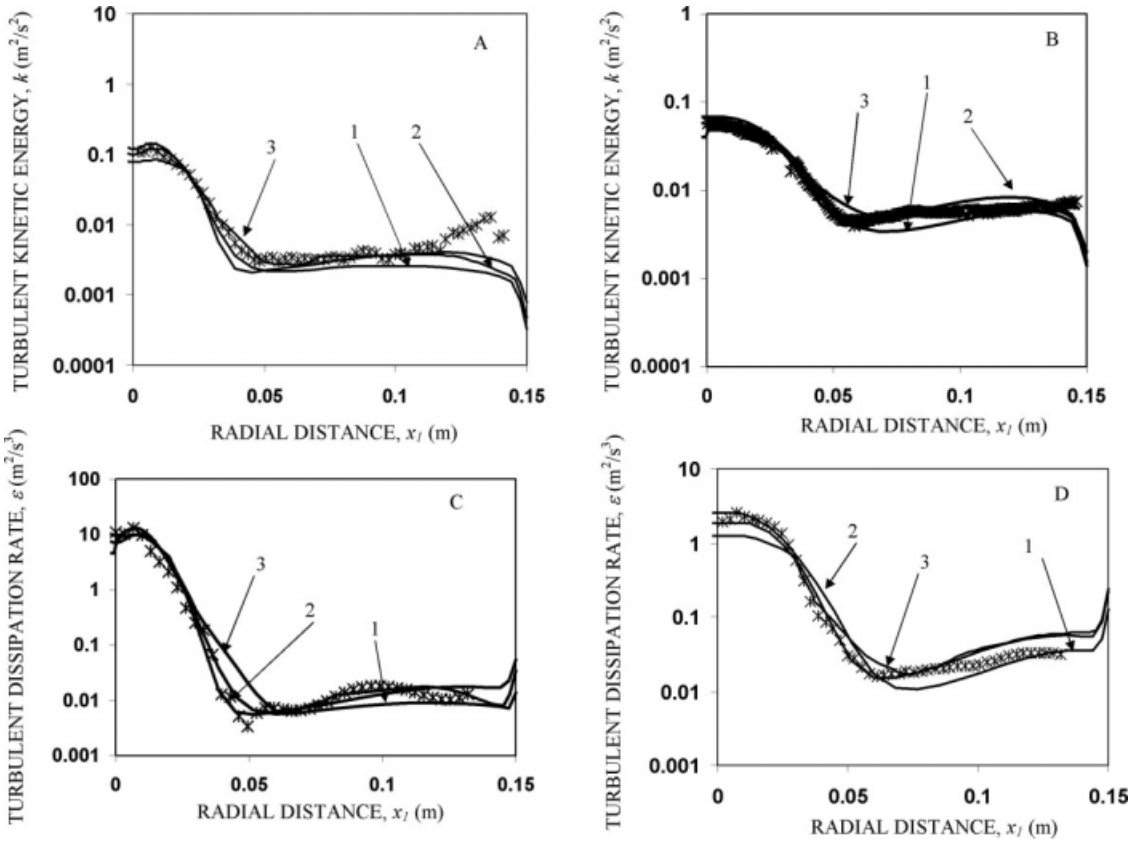

Figure 4. Radial profiles of turbulence Quantities for flow rate of 0.542 kg/s.

(A) Radial profiles of turbulent kinetic energy at $x_2 = 0.2$ m; (B) radial profiles of turbulent kinetic energy at $x_2 = 0.1$ m; (C) radial profiles of turbulent energy dissipation rate at $x_2 = 0.2$ m; and (D) radial profiles of turbulent energy dissipation rate at $x_2 = 0.1$ m: 1 k-ε model; 2 RSM; 3 LES model; *PIV Results.

literature have been extended to JLR (three-dimensional flow) by assigning same model constants over a horizontal plane (constant x_2). Figures 5C and D show variation of the flow characteristics for each of the model at $x_2 = 0.1$ m. Though these models have been found to be better for the case of round jets, they failed to predict the flow in JLR. One of the possible reasons is higher gradient in JLR resulting into deviation in the mean flow as well as turbulence parameters. It is observed that the model proposed by Rodi[31] perform well for axial velocity (deviation 10%; line 3), whereas higher deviations were observed for McGuirk and Rodi[29] (29%; line 4) and Morse[30] (32%; line 5) model. The modifications have been made by checking the sensitivity of each of the model constants in the model and based on the analysis suitable coefficients have been set to obtain the correct centerline velocity. Table 2 (columns 5 and 6) show the details of the parameter values for each model that suites the above mentioned condition. It has been observed that the radial spread of the jet is more in the case of each of the models (Figure 5C) as well as significant discrepancy (McGuirk and Rodi,[29] 202%; Morse,[30] 189% and Rodi,[31] 93%) can be observed in radial velocity profiles (Figure 5D). Hence, the turbulent quantities are not reported here. Thus, it can be concluded that the models proposed by McGuirk and Rodi,[29] Morse[30] as well as Rodi[31] are not suitable for JLR.

The model proposed by Pope[27] with $C_{\varepsilon 3} = 20$ (line 5, Figure 6) was found to deviate from experimental data whereas decreasing the value of $C_{\varepsilon 3}$ from 20 to 8 was found to give closer agreement to the experiments (line 4, Figure 6). It can be seen from the earlier discussion that the arbitrary manipulation of model parameters does not result into satisfactory predictions. This signifies the necessity to check the sensitivity of these parameters by keeping the other turbulence parameters to be constant.

To incorporate variation of C_μ, a model proposed by Basara and Jakirlić[32] has been used which is essentially a revised RSM. They have solved transport equations for Reynolds stresses. In stead of incorporating these stresses into mean flow equation, they have used eddy viscosity hypothesis (Eq. 5) to substitute $\langle u_i' u_j' \rangle$ in the mean flow equation, i.e. the Reynolds stresses enter the mean flow equation solely through the constant C_μ.

In the present work, similar approach has been used to take into account local variation of C_μ. But instead of solving transport equations for Reynolds stresses, they were estimated from (Eq. 5) and C_μ was calculated using following relationship,

$$C_\mu = \frac{-\left\langle u_i' u_j' \right\rangle \frac{\partial \langle u_i \rangle}{\partial x_j}}{\frac{k^2}{\varepsilon} \left| S_{ij} \right|^2} \tag{27}$$

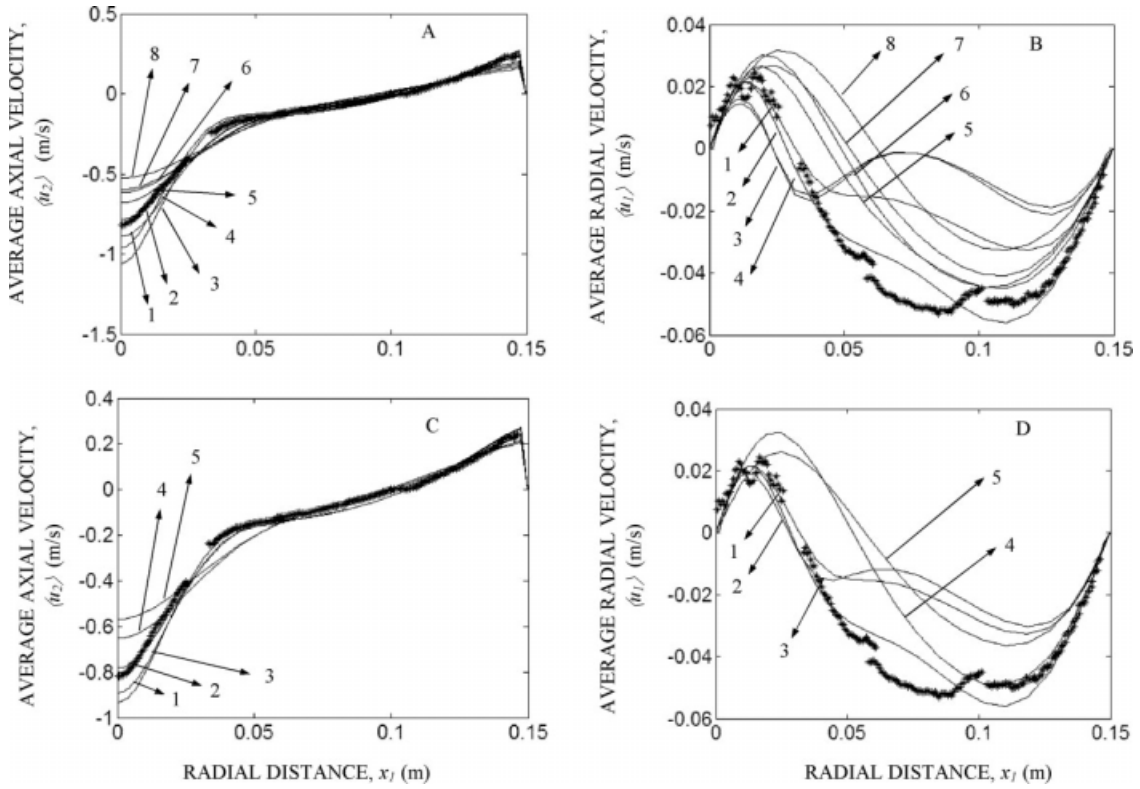

Figure 5. Radial profiles of $\langle u1 \rangle$;, $\langle u2 \rangle$, k and ε for the flow rate of 0.542 kg/s at $x_2 = 0.1$ m.

(A) Axial velocity profile; (B) radial velocity profile: 1 standard k-ε model; 2 RSM; 3 $C_{\varepsilon 2} = 1.8$; 4 $C_\mu = 0.05$; 5 $C_{\varepsilon 2} = 2.1$; 6 $C_\mu = 0.135$; 7 $C_{\varepsilon 1} = 1.3$; 8 $C_{\varepsilon 1} = 1.3$; and $C_\mu = 0.135$; *PIV Results. (C) Axial velocity profile; (D) Radial velocity profile: 1 standard k-ε model; 2 RSM; 3 Rodi[31]; 4 McGuirk and Rodi[29]; 5 Morse[30]; *PIV Results.

This procedure was repeated iteratively till the convergence was obtained. Furthermore, vorticity invariance term as proposed by Pope[27] has been added in the ε equation (Table 2). Equations 5 and 27 and the formulation of Pope[27] have been used as a hybrid model and it was expected to perform better than the standard k-ε model. This claim is based on the basis of two points. First, by iteratively calculating the local values of C_μ on the basis of local stress strain relationship, the local production term is modified appropriately accounting the anisotropic transfer. Second, incorporation of the additional term in the form of vorticity invariance makes the solution stable by accounting the effect of turbulence transport from production to dissipation.

Figures 6A-D show the predictions obtained by the hybrid model at $x_2 = 0.1$ m. The predictions have been found to be relatively better for the axial and especially radial component of velocity. The deviations for axial velocity are standard k-ε model, 17% (line 1); Pope's model ($C_{\varepsilon 3} = 8$), 6% (line 4); hybrid model, 6% (line 6). For radial velocity: standard k-ε model, 30% (line 1); Pope's model ($C_{\varepsilon 3} = 8$), 57% (line 4); hybrid model, 27% (line 5; Figure 6). In particular, turbulent kinetic energy and dissipation rate have been predicted relatively better than the other models. Turbulent kinetic energy: standard k-ε model, 8% (line 1); Pope's model ($C_{\varepsilon 3} = 8$), 13% (line 4); Hybrid model, 7% (line 5) and energy dissipation rate: standard k-ε model, 43% (line 1); Pope's model ($C_{\varepsilon 3} = 8$), 42% (line 4); Hybrid model, 37% (line 5).

Hence, hybrid model based on stress-strain relationship for the estimation of C_μ coupled with the modification of ε equation with vorticity invariance term has been proved to be a better option.

Analysis of the relative success of turbulence models

As discussed in the earlier section, standard k-ε model predictions were generally found to be relatively poor for axial velocity in the central region away from nozzle, radial velocity almost everywhere, turbulent kinetic energy and dissipation rate in the bulk and wall regions. On the other hand, LES and RSM were found to give better flow predictions. The relative poor performance of the k-ε model obviously originates from the simplifying assumptions. To understand the quantitative impact of these assumptions, it was thought desirable to estimate the production and transport terms (at least from the contribution of large scale structures) using LES, which are modeled in the standard k-ε model. For the mass flow rate of 0.542 kg/s, the Kolmogorov length scale was 26 μm and subgrid filter length scale was 2.2 mm with 2.5 million grid size. From the energy spectrum, it was found that 89% of the energy was in large scales, which were resolved and only 11% energy was modeled as subgrid scales. So, the production and transport terms obtained from LES can be used to cross check the modeling assumptions in the k-ε model. The comparison of production and transport terms estimated from LES and modeled terms in k equation

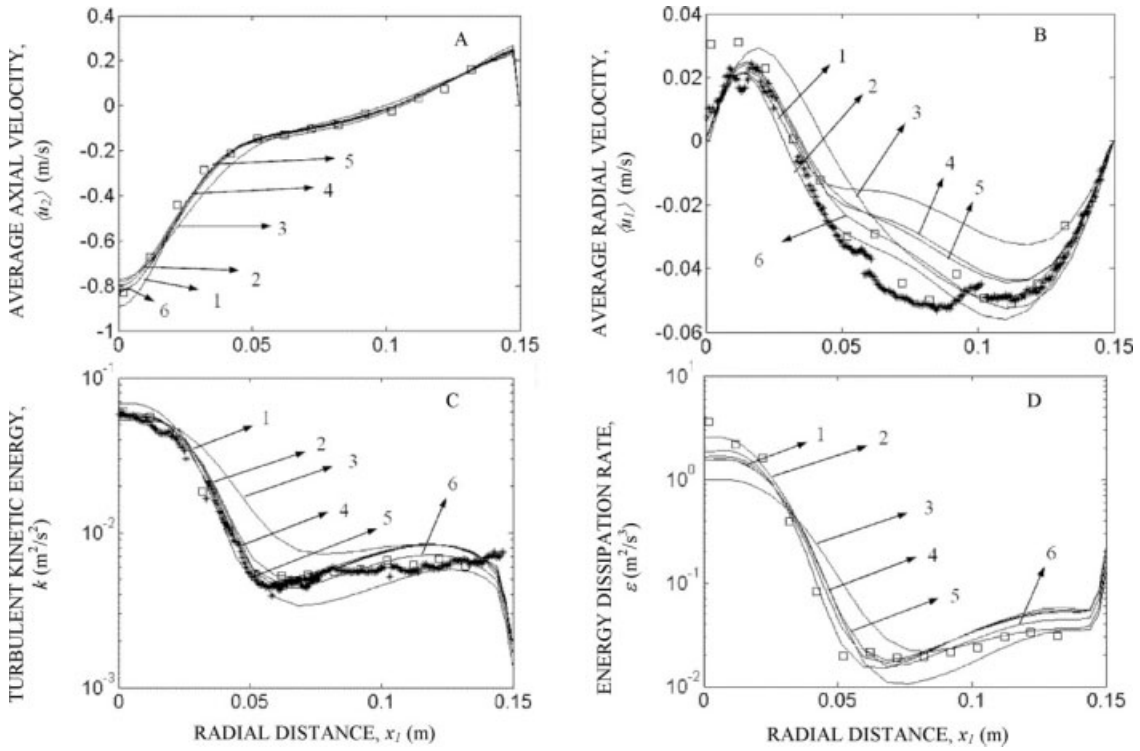

Figure 6. Radial profiles of $\langle u1 \rangle$, $\langle u2 \rangle$, k and ε from modified models for the flow rate of 0.542 kg/s at $x_2 = 0.1$ m.

(A) Axial velocity profile; (B) radial velocity profile; (C) turbulent kinetic energy profile; (D) energy dissipation rate profile: 1 standard k-ε model; 2 RSM; 3 modified model based on Morse[30]; 4 Modified model based on Pope[27] $C_{\varepsilon 3} = 8.0$; 5 Modified model based on Pope[27] $C_{\varepsilon 3} = 20.0$; 6 Modified hybrid model. *PIV Results.

is shown in Figures 7A and B, respectively. For instance, the production term $(-\rho\langle u_i' u_j' \rangle(\partial\langle u_i \rangle/\partial x_k)$, line 1 in Figure 7A) is modeled (as $\tau_{ij}\left(\partial\langle u_i \rangle/\partial x_j\right)$, line 2 in Figure 7A) considering flow to be isotropic, turbulent transport $\left(\partial\langle p' u_k' \rangle/\partial x_k\right)$ due to pressure fluctuation is neglected, triple correlations of velocity fluctuation $(\partial\left((-1/2)\rho\langle u_i' u_i' u_k' \rangle\right)/\partial x_k$, line 1 in Figure 7B) are modeled using gradient diffusion hypothesis $(\partial((\mu_t/\sigma_k)(\partial k/\partial x_k))/\partial x_k$, line 2 in Figure 7B)) and the model constants have been found for simple flows. The modeled production term can be seen to be 3 orders of magnitude higher than that obtained from LES (Figure 7A). The modeled transport was almost two orders of magnitude higher than actual transport (Figure 7B). The order of magnitude analysis of these two terms indicates that the production and transport try to compensate out each other to some extent. Whatever excess production remains, has been taken care by manipulation of C_μ, $C_{\varepsilon 1}$, and $C_{\varepsilon 2}$. The modifications in standard parameters in literature were able perform well to some extent because of the fact that an increase/a decrease in C_μ, $C_{\varepsilon 1}$, and $C_{\varepsilon 2}$ produced higher ε values and compensating the excess production, keeping the turbulent viscosity $(\mu_t = C_\mu \rho k^2/\varepsilon)$ bounded. Figures 7C and D show the comparison of modeled production and transport terms using the modified k-ε model available in the literature. It can be clearly seen that the modeled terms are orders of magnitude higher than those estimated by LES, but these modeled terms numerically compensate each other. This may be one of the reasons for the somewhat better agreement of modified k-ε models including the hybrid model used in the present work with the experimental data. Literature efforts can be considered as empirical due to insufficient knowledge about turbulence production, transport and dissipation in complex flows. So, the problem in modeled production term were attempted to resolve through dissipation equation rather than addressing the problem of turbulence production.

As the k-ε model assumes isotropy of the flow, all the normal stresses are equal in magnitude. This assumption is not valid for the case of JLR. The pressure strain terms obtained from RSM simulation show that there is significant redistribution of energy between the normal stresses in the central region. The terms Π_{11}, Π_{22}, and Π_{33} are compared at three axial locations $x_2 = 0.1$, 0.2, and 0.28 (Figures 8A-C). The redistribution is very high close to the nozzle and it goes on decreasing away from the nozzle. However, we would also like to admit that the pressure strain can not be the only major governing factor, as RSM results of radial velocity were found to be deviating at an axial location of $x_2 = 0.2$. All other quantities are in good agreement at both the axial locations $x_2 = 0.1$ and 0.2.

Hence, it can be concluded that, any modifications to standard k-ε model, can not represent the real complex flows, though can provide reasonably accurate velocities and turbulence quantities.

Simulation time

In case of standard k-ε model, RSM and hybrid models the explicit termination criteria was identical and it was the reduction of global residual below 10^{-4} for all equations, i.e., momentum, pressure, turbulent kinetic energy, turbulent

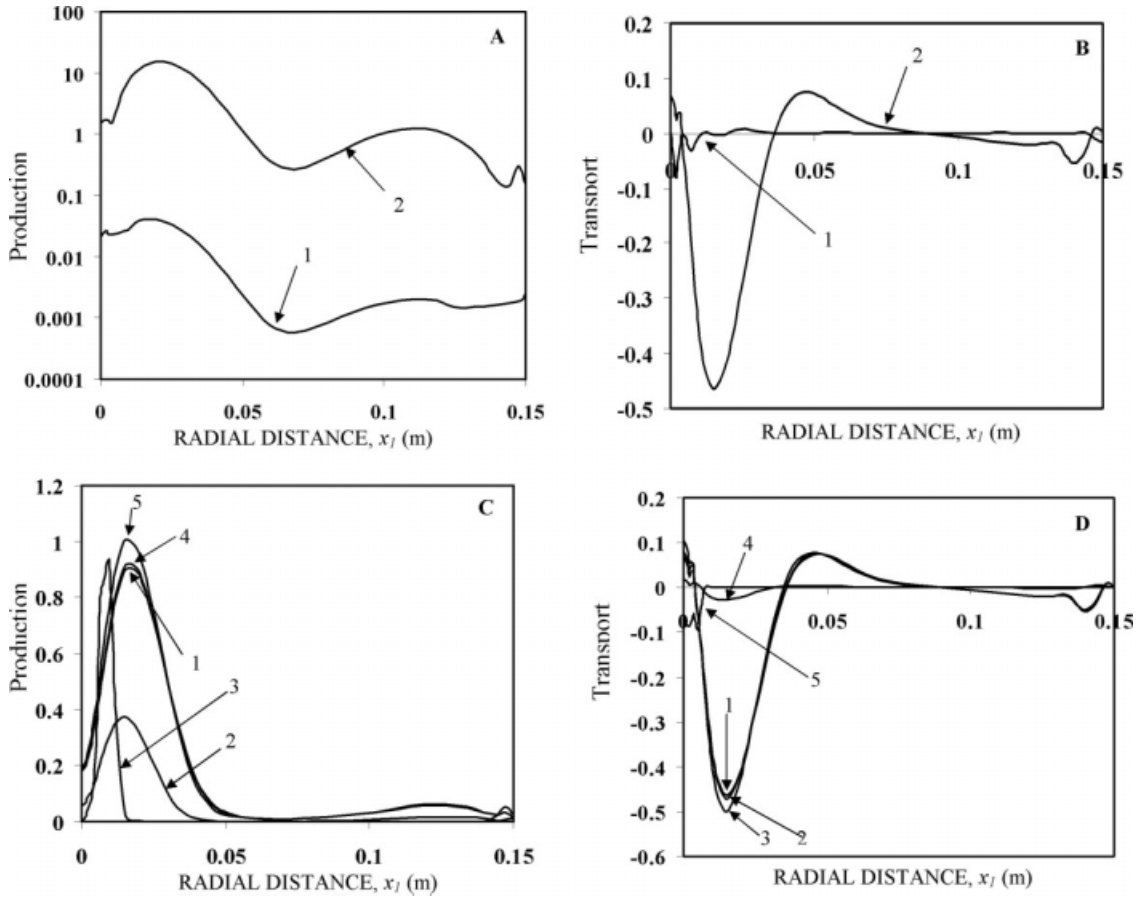

Figure 7. Comparison of turbulence production and transport term in turbulent kinetic energy equation in JLR.

(A) turbulent kinetic energy production term using standard k-ε model and LES: 1 LES; 2 standard k-ε model. (B) Turbulent kinetic energy transport term using standard k-ε model and LES: 1 standard k-ε model; 2 LES. (C) Turbulent kinetic energy production term using modified k-ε models: 1 standard k-ε model; 2 Rodi[31]; 3 Hybrid model; 4 Pope[27] $C_{\varepsilon 3} = 8.0$; 5 Pope[27] $C_{\varepsilon 3} = 20.0$. (D) Turbulent kinetic energy transport term using modified k-ε models: 1 standard k-ε model; 2 Rodi[31]; 3 Hybrid model; 4 Pope[27] $C_{\varepsilon 3} = 8.0$; 5 Pope[27] $C_{\varepsilon 3} = 20.0$.

dissipation rate, and Reynolds stresses. LES simulations were carried out with a time step of 5×10^{-4} s for 40,000 time steps. The k-ε and RSM simulations were carried out on the grid size of 0.6 million and LES simulations were carried out on grid size of 0.6 and 2.5 million grid size. For hybrid model, the under-relaxation parameter for continuity had to be reduced from 0.45 (standard k-ε model) to 0.25. Initial 300 iterations were carried out using standard k-ε model and later model was changed to hybrid model. This was necessary for avoiding the divergence problem in the simulation. The details of two computational facilities used are (i) SGI dual processor compute node (8 compute cores with 4 GB RAM) and (ii) AMD Opteron 2 processor node with 2 GB RAM. The details of the computational time are provided in Table 3.

CFD modeling of hydrofoil impeller

The favorable performance of the hybrid k-ε model in JLR has motivated us to test it for the other type of geometry with similar kind of flow. The model has been applied to STR with hydrofoil impeller (Np $\sim$ 0.27). Among all the impeller designs, hydrofoils provide better convection.[38] Hence, hydrofoil impellers offer relatively better macromixing characteristics than any other type of impeller design. To have direct comparison with the JLR, the equal power input (same as for the case of 0.542 kg/s $\sim$ 6.5 W/kg) has been selected as the basis for simulation.

For the STR simulation, the cylindrical vessel of diameter $T = 0.30$ m and height $H = 0.40$ m was used. The diameter of the impeller was $d_i = T/3$. The impeller has been kept at $H_C/T = 0.33$. The impeller rotational speed was 6.67 rps and water was used as the working fluid. Hexahedral elements were used for meshing the geometry and a good quality of mesh is ensured throughout the computational domain using GAMBIT mesh generation tool. To ensure better quality mesh, impeller blades and baffles have been considered with zero thickness. The computational mesh consists of 0.3 million hexahedral cells.

Figures 9A-F show the comparison of hybrid as well as standard k-ε model with the inhouse laser Doppler velocimetry (LDV) measurements at two axial locations $x_2 = 0.13$ m and $x_2 = 0.30$ m. The predictions obtained by hybrid k-ε model have been found to be excellent for the axial and

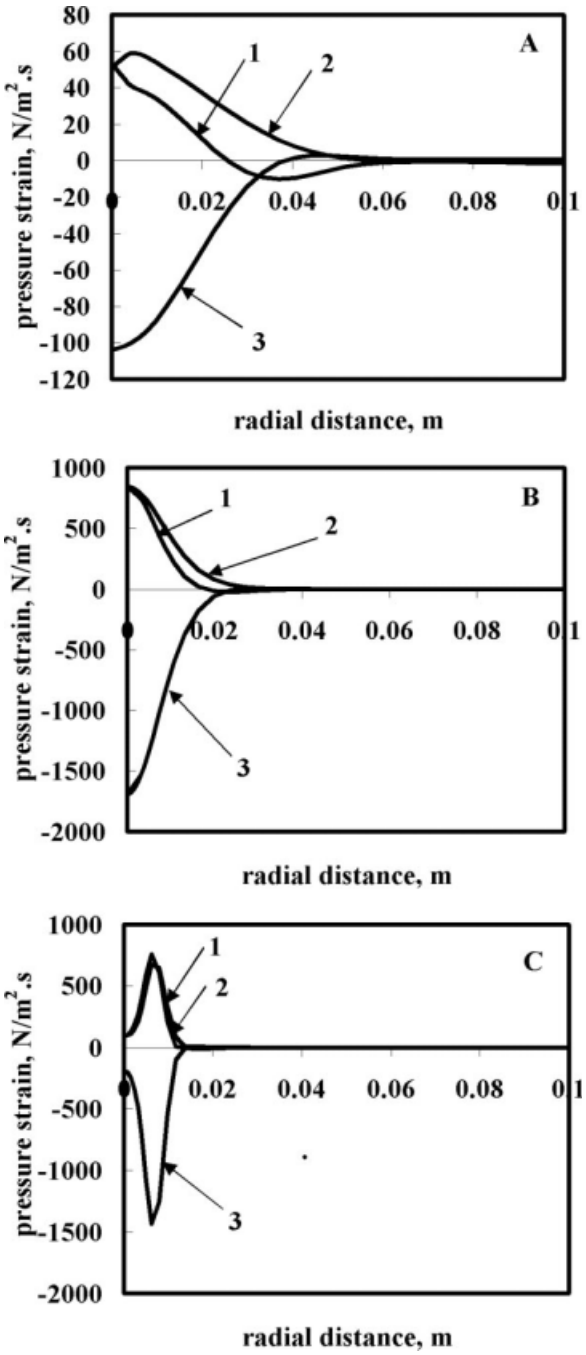

Figure 8. Comparison of pressure strain term in JLR at x_2 = 0.1, 0.2, and 0.28 m.

(A) Radial variation of pressure strain at $x_2 = 0.1$ m. (B) Radial variation of pressure strain at $x_2 = 0.2$ m. (C) Radial variation of pressure strain at $x_2 = 0.28$ m. Line 1: Π_{11}, Line 2: Π_{22}, and Line 1: Π_{33}.

especially the radial component of velocity (axial velocity: standard k-ε model, 16%; hybrid k-ε model, 7% and radial velocity: standard k-ε model, 23%; hybrid k-ε model, 7%) at $x_2 = 0.13$ m (Figures 9A and C). The deviations were found to increase with an increase in x_2. At $x_2 = 0.3$ m, hybrid k-ε model showed deviation of 14% for axial velocity and 23% for radial velocity (Figures 9B and D). Figures 9E and F show the comparison for turbulent kinetic energy, and it can be seen that turbulent kinetic energy has been predicted substantially better by the hybrid k-ε model compared with standard k-ε model (at $x_2 = 0.13$ m, standard k-ε model, 19%; hybrid k-ε model, 11% and at $x_2 = 0.13$ m, standard k-ε model, 26%; hybrid k-ε model, 5%). With this understanding of flow in STR, simulations have been further extended to estimate the mixing time in JLR and STR using the hybrid k-ε model.

Mixing efficiency of JLR versus STR

It was thought desirable to compare the macromixing efficiency of JLR with STR provided with a hydrofoil impeller. The comparison has been made for four cases and at the same power consumption per unit volume namely (i) hydrofoil impeller having diameter $d_i = 0.1$ m, and three cases of JLR with (ii) $d = d_i$, (iii) $d = d_i/2$ and (iv) $d = d_i/5$. To begin with, an attempt has been made to understand the flow pattern in both the systems. Dominant axial convective flow is a key feature of both the systems. Figure 10 shows the vector plots for the four cases. Flow generated by a jet (Figures 10B-D) is vertically downward at 0° (practically no radial component) and spreads with a cone angle of 14° (Figures 10 C and D); whereas, hydrofoil generates (Figure 10A) mixed flow with starting vectors having an angle of around 20° (to the vertical) and spreads with a cone angle of 30°. A small circulation cell is formed below the impeller which is not present in the case of a jet. The primary eye of the mean circulation flow can be seen at $x_1 = 0.12$ m, $x_2 = 0.123$ m and the secondary eye at $x_1 = 0.035$ m, $x_2 = 0.042$ m. Furthermore, for the case of jet having a diameter of d_i (Figure 10B), primary eye of the circulation cell was found to be at $x_1 = 0.095$ m and $x_2 = 0.29$ m i.e. at the level of the nozzle itself. For case (iii) (Figure 10C), the jet length was found to be longer than the case (ii). Similarly, the primary eye of the circulation was also found to be shifted to a lower location of $x_1 = 0.1$ m and $x_2 = 0.12$ m. On the other hand, for case (iv) (Figure 10D), the flow pattern shows the primary eye at $x_1 = 0.06$ m and $x_2 = 0.1$ m. Also, a start of the secondary eye was observed above the nozzle whose center was at $x_1 = 0.11$ m and $x_2 = 0.35$ m.

Before estimating the macromixing efficiency, it was thought desirable to estimate the convective flow in four cases. A horizontal plane was created at $x_2 = 0.15$ m and in this plane total upward flow (positive axial velocity) has been calculated, this upward flow is the circulation flow. Then average circulation velocity was calculated from the area of upward flow. In JLR, two circulation loops are formed. The length of circulation loop was estimated as $(2 \times H \times D/2)$. The ratio of circulation length to circulation velocity is circulation time. For this purpose, the values of circulation flow were estimated for the cases (i) and (iv) and were found to be 0.0062, 0.0093, 0.0081, and 0.0067 m^3/s, respectively. Thus, in the case of JLR, the convective flow is relatively more than that of hydrofoil impeller.

From the knowledge of flow pattern, the values of mixing time were estimated by solving the scalar transport equation:

$$\frac{\partial\langle c\rangle}{\partial t} + \langle u_j\rangle \frac{\partial\langle c\rangle}{\partial x_j} = \frac{\partial}{\partial x_j}\left((D_m + D_t)\frac{\partial\langle c\rangle}{\partial x_j}\right) \qquad (28)$$

Table 3. Computational time for various turbulence models

S.No.	Model	No. of Grid Points (in million)	No. of Iterations/Time Steps	AMD Opteron Machine	SGI Macine
1	Standard k-ε model	0.6	5600 iterations	5 hr	3.5 hr
2	Reynolds stress model	0.6	8400 iterations	8 hr	5.5 hr
3	Hybrid k-ε model	0.6	11,300 iterations	7 hr	5 hr
4	LES (coarse)	0.6	40,000 time steps	54 days	22 days
5	LES (fine)	2.5	40,000 time steps	–	35 days

where,

$$D_m = \upsilon/Sc, \tag{29}$$

$$D_t = \upsilon_t/Sc_t. \tag{30}$$

The value of Sc was taken as 1000 for all the simulations. The turbulent Schmidt number was selected as 0.9, which was found in accordance with the values observed by Ekambara and Joshi.[39] The tracer was injected radially near the center ($x_1 = 0.02$ m) and near top surface ($x_2 = 0.38$ m) and with initial normalized concentration $C_0 = 1$ and tracer volume to be approximately 1% of the total volume of the bath liquid. The time step was kept very small (10^{-4} s), when the concentration gradients are very large. The convergence criterion for the residual in Eq. 28 was set to be 10^{-8}. Mixing time was considered to be a time at which the concentration at all the locations is within 1 per cent of the homogenization.

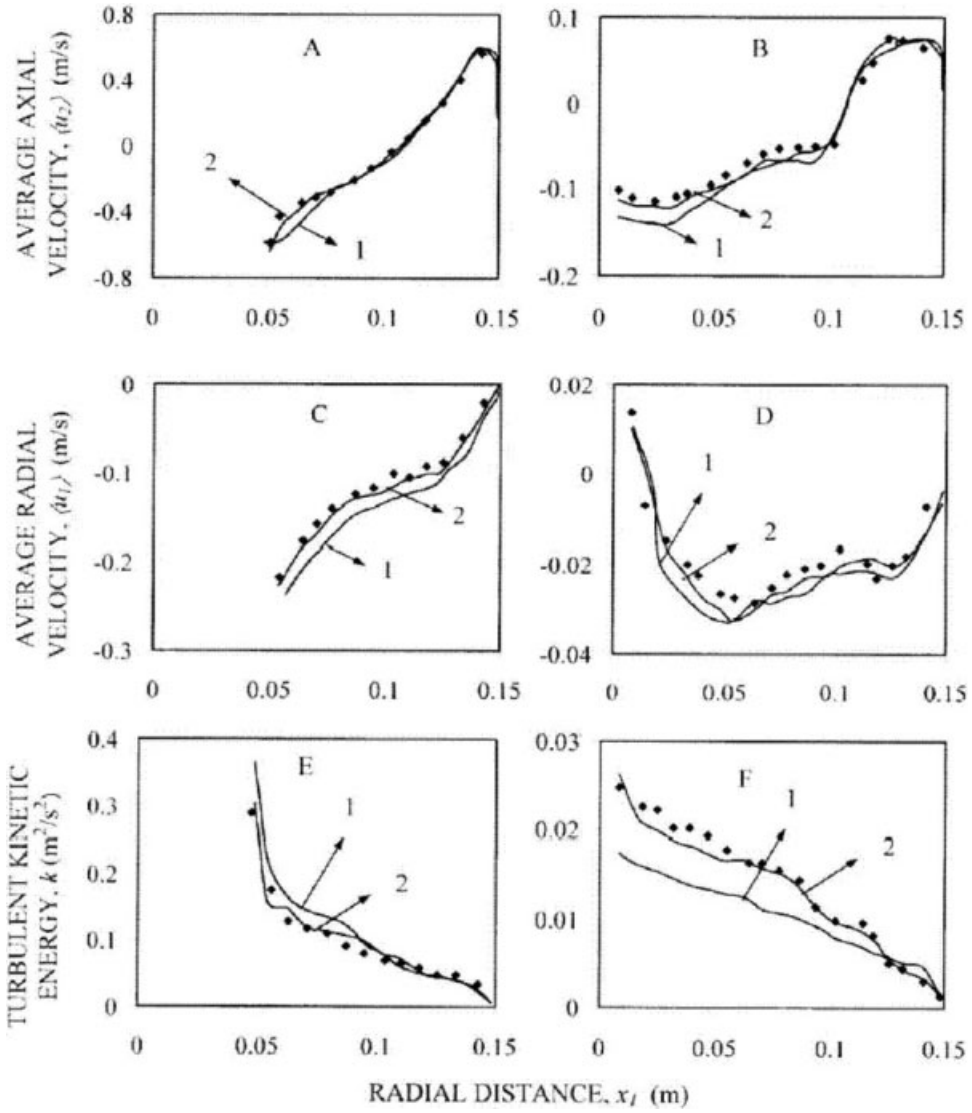

Figure 9. Radial profiles of $\langle u1 \rangle$, $\langle u2 \rangle$ and k for hydrofoil impeller.

(A) Axial velocity profile at $x_2 = 0.13$ m; (B) Axial velocity profile at $x_2 = 0.3$ m; (C) Radial velocity profile at $x_2 = 0.13$ m; (D) Radial velocity profile at $x_2 = 0.3$ m; (E) Turbulent kinetic energy profile at $x_2 = 0.13$ m; (F) Turbulent kinetic energy profile at $x_2 = 0.3$ m; 1 standard k-ε model; 2 Modified hybrid model (present model); ♦ LDV Results.

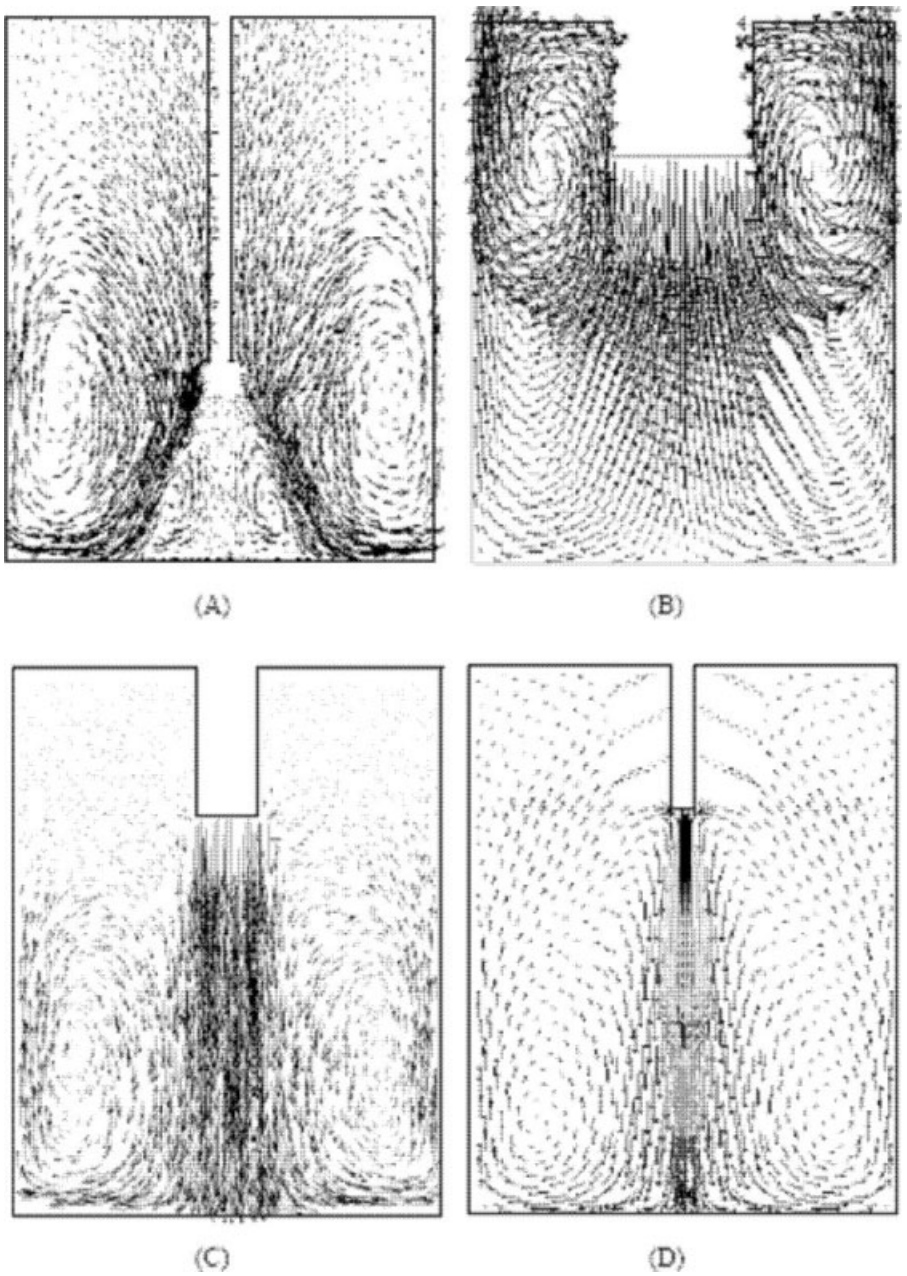

Figure 10. Vector plots for jet flows and flows generated by hydrofoil impeller.

(A) Hydrofoil impeller, $d_i = 0.1$ m; (B) Nozzle of $d = d_i$; (C) Nozzle of $d = d_i/2$; and (D) Nozzle of $d = d_i/5$.

For the above four cases (i)-(iv), the values of mixing time were found to be 10.9, 6.7, 8.1, and 12.2 s, respectively. It can be seen that the JLR can give much lower mixing time (by about 40%) for $d = d_i$. However, for the case of smallest jet diameter, the mixing time is even higher than the impeller case. It is reminded at this stage that the circulation flow rates for JLR ($d = d_i/5$) and STR are 0.0067 and 0.0062 m^3/s, respectively. Though the JLR [case (iv)] generates higher convective flow it gives high mixing time. This is because the mixing is not completely governed by the mean flow. For efficient mixing, an appropriate combination of mean flow and eddy diffusivity is required. This point has been explained in detail by Ekambara and Joshi[39] and Thakre and Joshi.[40] This section brings out the importance of the selection of jet diameter. An appropriate selection ($d = d_i$) gives 40% lower mixing time compared with STR, whereas ($d = d_i/5$) gives 12% higher mixing time. Thus, it can be seen that the JLR can be inferior to STR and proper selection of the nozzle diameter is important.

Conclusions

In the present work, flow in JLR has been simulated using various turbulence modeling approaches such as standard k-ε model, RSM and LES. Also measurements have been made using PIV. The conclusions are as follows:

1. The experiments have been carried out using PIV to measure the mean flow pattern and the turbulence quantities for jet loop reactor. A structure function based methodology has been used to estimate the turbulent dissipation rate using the PIV data.

2. The k-ε based simulations reported in the literature have been critically analyzed. In all the suggested methods, modifications have been made in the values of model parameters depending on the values of local flow parameters. In this work, parametric sensitivity of all these parameters has been investigated in practically all the regions of JLR. Then it was found that the introduction of one more turbulence parameter ($C_{\varepsilon 3}$) as proposed by Pope[27] was found to be useful.

3. From the comparison of standard k-ε model, RSM and LES, failure of various k-ε models can be attributed to inability to predict production and transport terms accurately. It was found that, all the modified k-ε models were in serious error and the effect of excessive modeled production was taken care by manipulation of C_μ, $C_{\varepsilon 1}$, and $C_{\varepsilon 2}$. It was observed that the modeled terms are orders of magnitude higher than those estimated for LES, but these modeled terms numerically compensate each other. The problems in modeled production term were attempted to resolve through dissipation equation rather than addressing the problem of turbulence production.

4. RSM simulations have shown a significant redistribution of turbulent kinetic energy (through pressure strain term) between normal stresses in the central region. Because of inherent assumption of isotropy, such a feature can not be captured by any k-ε models, which can also be one of the reasons of failure of k-ε models in comparison with RSM and LES.

5. A modified model has been suggested based on the implicit stress relationship for the better estimation of C_μ (Basara and Jakirlić[32]) and $C_{\varepsilon 3}$ in the ε equation (Pope[27]). The hybrid model showed better performance as compared to all the models reported in the literature. Simulation time for hybrid model was higher than standard k-ε model and almost comparable with that of RSM.

6. The hybrid k-ε model was also used for the simulation of stirred tank reactor with hydrofoil impeller (Np $\sim$ 0.27). The simulation results were in good agreement with the experimental data.

7. The effect of nozzle diameter on mixing time has been investigated at the same power consumption ranging from d_i *to* $d_i/5$. In view of strong influence of nozzle diameters, it has been shown that the JLR can be inferior to STR if proper nozzle diameter is not selected.

Notation

$A_{f\mu}$, A_{f2}, A_1, A_2 = model equation multiplying constants (Table 2)
$\langle c \rangle$ = tracer concentration in frozen field study from RANS model (mol/m^3)
C = constant in the second order structure function
C_0 = dimensionless initial concentration
C_1 = empirical constant in Eq. 13
C_2 = empirical constant in Eq. 14
C_d = empirical constant in Eq. 21
C_{ij} = convective term in Eq. 15
C_l = empirical constant in Eq. 16
C_S = Smagorinsky constant
$C_{w,1}$ = empirical constant in Eq. 16
$C_{w,2}$ = empirical constant in Eq. 16
$C\varepsilon$ = empirical constant in Eq. 22
$C_{\varepsilon 3}$ = empirical constant (Table 2)
$C_{\mu,}$, $C_{\varepsilon 1}$, $C_{\varepsilon 2}$ = constants in k-ε turbulence model
d = nozzle diameter (m)
d_i = diameter of impeller (m)
D = tank diameter (m)
D_m = molecular diffusion coefficient (m^2/s)
D_t = turbulent diffusion coefficient (m^2/s)
D_{uu} = second order velocity structure function (m^2/s^2)
D_{uuu} = third order velocity structure function (m^3/s^3)
e_{f}, e_1 = constants in modeled equations in Table 2.
f = model constant proposed by Rodi[29]
fr = frequency in the FFT (Hz)
H = liquid height (m)
H_C = clearance height (m)
H_N = Distance of nozzle from bottom, (m)
k = turbulent kinetic energy (m^2/s^2)
k_{sgs} = turbulent kinetic energy (m^2/s^2)
l = length scale magnitude $= \kappa^{-1}$, (m)
L = turbulent length scale (m)
n_k = unit normal vector in Eq. 16
N_p = power number
p_i = pressure (N/m^2)
P_{ij} = production term in Eq. 15 (N/m^{2}s)
p_{sgs} = subgrid scale pressure (N/m^2)
$\overline{p}$ = filtered pressure term for LES model (N/m^2)
p' = fluctuating pressure (N/m^2)
$\langle \mathrm{p_i} \rangle$ = time averaged pressure (N/m^2)
$\mathcal{P}$ = Production term in the ε equation (Table 2) $= \tau_{ij} \frac{\partial \langle u_i \rangle}{\partial x_j}$ (N/m^{2}s)
Q = volumetric flow rate (m^3/s)
$r_{1/2}$ = distance from center line to the location when velocity is half that of $\langle u_{2,\not\subset} \rangle$, centerline velocity (m)
r_D = difference in the two locations for calculation of structure function (m)
r'_D = variable within an integration representing the difference in the two locations for calculation of structure function (m)
S_{ki} = shear rate (s^{-1}) $= \frac{1}{2}\left(\frac{\partial \langle u_k \rangle}{\partial x_i} + \frac{\partial \langle u_i \rangle}{\partial x_k}\right)$
$\overline{S_{ij}}$ = shear rate in resolved velocity field in LES model (s^{-1})
$\left|\overline{S_{ij}}\right|$ = magnitude of shear rate in LES model (s^{-1}) $= \sqrt{2\,\overline{S_{ij}}\,\overline{S_{ij}}}$
Sc = Schmidt number
Sc_t = turbulent Schmidt number
t = time (s)
t_s = turbulent time scale (s)
T = Tank diameter (m)
u = velocity scale (m/s)
u_i = instantaneous velocity of component i, where i = 1,2,3 corresponds to radial, axial and tangential component of velocity (m/s)
$u_{i,\mathrm{sgs}}$ = subgrid-scale velocity of component i (m/s)
u'_i = fluctuating part of velocity of component i (m/s)
$\overline{u_i}$ = filtered velocity of component i for LES model (m/s)
$\langle u_i \rangle$ = time average of velocity (m/s)
$\langle u_{2,J} \rangle$ = nozzle velocity (m/s)
$\langle u_{2,\not\subset} \rangle$ = centerline velocity (m/s)
V = volume (m^3)
V_C = circulation velocity (m/s)
x_i = co-ordinate distances in i direction where i = 1,2,3 (m)

Greek letters

χ = normalized invariance; (Parameter defined in Table 2)= $\omega_{ij}\omega_{jk}S_{ki}$
δ_{ij} = Kronekar delta = 1 if $i = j$; = 0 if $i \neq j$
δ_j = width of shear region in Table 2 (m)
Δ = LES filter scale (m)
$\Delta\langle u_2 \rangle$ = maximum velocity difference across the jet in Table 1 (m/s)
ε = energy dissipation rate (m^2/s^3)
$\varepsilon_{\mathrm{sgs}}$ = sub-grid scale energy dissipation rate (m^2/s^3)
η = Kolmogorov length scale (m)

λ = Taylor microscale (m)
μ = dynamic viscosity (kg/ms)
μ_{sgs} = subgrid scale viscosity (kg/ms)
μ_t = turbulent viscosity (kg/ms)
υ = kinematic viscosity (m^2/s)
υ_{sgs} = subgrid scale viscosity (m^2/s)
υ_t = eddy viscosity (m^2/s)
Π_{ij} = pressure strain tensor, (N/m^2s)
$\Pi_{ij,rapid}$ = rapid term in pressure strain tensor, (N/m^2s)
$\Pi_{ij,slow}$ = slow term in pressure strain tensor, (N/m^2s)
$\Pi_{ij,wall}$ = wall reflection term in pressure strain tensor, (N/m^2s)
ρ = density of liquid (kg/m^3)
σ_k = parameter in k-ε model
σ_ε = parameter in k-ε model
τ_{ij} = Reynolds Stress (m^2/s^2) = $-\langle u_i' u_j' \rangle$
$\overline{\tau}_{ij}$ = sub grid scale Stress (m^2/s^2) = $-\overline{u_i' u_j'}$
ω_{ij} = vorticity tensor (s^{-1}) = $\frac{1}{2}\left(\frac{\partial\langle u_i\rangle}{\partial x_j} - \frac{\partial\langle u_j\rangle}{\partial x_i}\right)$

Subscript and superscript

$\not\subset$ = variable at centerline
i, j, k = coordinates in generalized form with value 1, 2 and 3 corresponds to radial, axial, and tangential direction
J = variable value at nozzle exit
$'$ = fluctuating component
$-$ = LES-filtered component

Acknowledgments

C. S. Mathpati and Sagar Deshpande acknowledge the financial support of Council of Scientific and Industrial Research and University Grant Commission, Government of India, respectively.

Literature Cited

1. Dihn TN, Bui VA, Nourgaliev RR, Green JA, Sehgal BR. Experimental and analytical studies of melt jet-coolant interactions: a synthesis. *Nuclear Eng Des*. 1999;189:299–327.
2. Oldshue JY. *Fluid Mixing Technology*. New York: Mcgraw Hill, 1983.
3. Simon M, Fonade C. Experimental study of mixing performances using steady and unsteady jets. *Can J Chem Eng*. 1993;71:507–513.
4. Forney LJ, Nafia N. Eddy contact model: CFD simulations of liquid reactions in nearly homogeneous turbulence. *Chem Eng Sci*. 2000; 55:6049–6058.
5. Baldyga J, Bourne JR, Zimmermann B. Investigation of mixing in jet reactors using fast competitive-consecutive reactions. *Chem Eng Sci*. 1994;49:1937–1946.
6. Pope SB. *Turbulent flows*. Cambridge: Cambridge University Press, 2000.
7. Hussein HJ, Capp SP, George WK. Velocity measurements in a high-Reynolds-number momentum-conserving, axisymmetric, turbulent jet. *J Fluid Mech*. 1994;258:31–75.
8. Panchapakesan NR, Lumley JL, Turbulence measurements in axisymmetric jets of air and helium. Part 1: Air jet. *J Fluid Mech* 1993;246:197–243.
9. Donald MB, Singer H. Entrainment in turbulent fluid jets. *Trans Inst Chem Eng*. 1959;37:255–267.
10. Rossler RS, Bankoff SG. Large-scale turbulence characteristics of a submerged water jet. *AIChE J*. 1963;9:672–676.
11. Sadakata M, Kunii D. Recirculation and turbulence by jet flow confined in vessel. *J Chem Eng Jpn*. 1972;5:355–360.
12. Usui H, SanoY. Turbulent structure of submerged jets of dilute polymer solutions. *J Chem Eng Jpn*. 1980;13:401–404.
13. Lane AGC, Rice P. The flow characteristics of a submerged bounded jet in a closed system, short communication. *Trans ICHEME Symp Ser*. 1982;64:245–248.
14. Yianneskis M. *The effect of flow rate and tracer insertion time on mixing times in jet agitated vessels*. In: *Proceedings of 7th European Conference on Mixing*, Kiav, Brugge, Belgium. 1991:121–128.
15. Mewes D, Renz R. *Jet mixing of liquids in storage tanks*. In: Proceedings of 7*th* European Congress on Mixing, Brugge, Belgium. 1991:131–137.
16. Nishimura T, Inaba S, Hishida K, Maeda M. *Measurements of flow around inclined jets by stereoscopic PIV*. In: Proceedings of 10*th* International Symposium on Applications of Laser Techniques to Fluid Mechanics, Lisbon. 2000.
17. Brooker L. Mixing with the jet set. *Chem Eng*. 1993;30:16.
18. Fossett H. The action of free jets in mixing of fluids. *Trans Inst Chem Eng*. 1951;29:322–332.
19. Lehrer IH. A new model for free turbulent jets of miscible fluids of different density and a jet mixing time criterion. *Chem Eng Res Des*. 1981;59:247–252.
20. Maruyama T, Ban Y, Mizushina T. Jet mixing of fluids in tanks. *J Chem Eng Jpn*. 1982;15:342–348.
21. Ranade VV. Towards better mixing protocols by designing spatially periodic flows: the case of a jet mixer. *Chem Eng Sci*. 1996;51:2637–2642.
22. Jayanti S. Hydrodynamics of jet mixing in vessel. *Chem Eng Sci*. 2001;56:193–210.
23. Patwardhan AW. CFD Modeling of jet mixed tanks. *Chem Eng Sci*. 2002;57:1307–1318.
24. Launder BE, Spalding DB. The numerical computation of turbulent flow. *Comput Methods Appl Mech Eng*. 1974;3:269.
25. Launder BE, Second-moment closure and its use in modeling turbulent industrial flows. *Int J Numer Methods Fluids*. 1989;9:963–985.
26. Kim WW, Menon S. *Application of the localized dynamic subgrid-scale model to turbulent wall-bounded flows*. In: *35th Aerospace Sciences Meeting*, Reno, NV, 1997. Technical Report AIAA-97-0210. American Institute of Aeronautics and Astronautics.
27. Pope SB. An explanation of turbulent round jet/plane jet anomaly. *AIAA J*. 1978;16:279–281.
28. Launder BE, Morse AP, Rodi W, Spalding DB. The prediction of free shear flows- a comparison of six turbulence models. *NASA Rep*. 1972;SP–311.
29. McGuirk JJ, Rodi W. The calculation of three dimensional free jet. In: Symposium on Turbulent Shear Flows, Pennsylvania State University, PA, 1977.
30. Morse AP. *Axisymmetric Turbulent Shear Flows With and Without Swirl*. Ph.D. Thesis. England: London University, 1977.
31. Rodi W. *Turbulence Models and Their Applications to Hydraulics*. Rotterdam: A.A. Balkema, 1993. IAHR/AIRH Monograph.
32. Basara B, Jakirlić S. A new hybrid turbulence modeling strategy for industrial CFD. *Int J Numer Methods Fluids*. 2003;42:89–116.
33. Lui S, Meneveau C, Katz J. On the properties of similarity subgrid-scale models as deduced from measurements in a turbulent jet. *J Fluid Mech*. 1994;275:83–119.
34. Ilyusin BB, Kranksky DV. Large eddy simulation of the turbulent round jet dynamics. *Thermophys Aeromech*. 2006;13:43–54.
35. Lindborg E. Correction to the four-fifth law due to variations of the dissipation. *Phys Fluids*. 1999;11:510–512.
36. Kang HS, Chester S, Meneveau C. Decaying turbulence in an active grid generated flow and comparisons with large eddy simulations. *J Fluid Mech*. 2003;480:129–160.
37. Deshpande SS, Sathe MJ, Joshi JB. Evaluation of Local Turbulent Energy Dissipation Rate using PIV in Jet Loop Reactor. *Ind Eng Chem Res*. 2009;48:5046–5057.
38. Sahu AK, Joshi JB. Simulation of flow in stirred vessels with axial flow impellers: effects of various numerical schemes and turbulence model parameters. *Indust Eng Chem Res*. 1995;34:626–639.
39. Ekambara K, Joshi JB. Axial mixing in pipe flows: turbulent and transition regions. *Chem Eng Sci*. 2003;58:2715–2724.
40. Thakre SS, Joshi JB. Momentum, mass and heat transfer in single phase turbulent flow. *Rev Chem Eng*. 2002;18:83–293.

Manuscript received Mar. 20, 2007, and revision received Jan. 7, 2009.